Unlocking Mitochondrial Dysfunction-Associated Senescence (MiDAS) with NAD$^+$ – a Boolean Model of Mitochondrial Dynamics and Cell Cycle Control

Herbert Sizek[a,†,1], Dávid Deritei[b,†], Katie Fleig[c], Marlayna Harris[a,2], Peter L. Regan,
Kimberly Glass[3], Erzsébet Ravasz Regan[1*]

[a] Biochemistry and Molecular Biology, The College of Wooster, Wooster, OH 44691, U.S.A.
[b] Channing Division of Network Medicine, Brigham and Women's Hospital / Harvard Medical School, Boston, MA 02115, U.S.A.
[c] Neuroscience, The College of Wooster, Wooster, OH 44691, U.S.A.

† *Co-first authors*
* *Corresponding author:* ERR, eregan@wooster.edu

Highlights

- Boolean regulatory network model reproduces mitochondrial dynamics during cell cycle progression, apoptosis, and glucose starvation.
- Model offers a mechanistic explanation for the positive feedback loop that locks in Mitochondrial Dysfunction-Associated Senescence (MiDAS), involving autophagy-resistant hyperfused but dysfunctional mitochondria.
- Model reproduces ROS-mediated mitochondrial dysfunction and suggests that MiDAS is part of the early phase of damage-induced senescence.
- Model predicts that cancer-driving mutations that bypass the G1/S checkpoint generally increase the incidence of MiDAS, with the notable exception of *p53* loss.

Declarations of interest: none

Abstract

The steady accumulation of senescent cells with aging creates tissue environments that aid cancer evolution. The secretome of senescent cells promotes chronic inflammation, contains growth and transforming signals, and causes chronic oxidative stress. The latter is primarily due to dysfunctional mitochondria often seen in senescent cells. Aging cell states are highly heterogeneous. 'Deep senescent' cells rely on healthy mitochondria to fuel a strong proinflammatory secretome. In parallel, the triggers of deep senescence also generate cells with mitochondrial dysfunction, and sufficient energy deficit to alter their secretome – a state termed Mitochondrial Dysfunction-Associated Senescence (MiDAS). Here we offer a mechanistic explanation for the molecular processes leading to MiDAS. To do this we have built a Boolean regulatory network model able to reproduce mitochondrial dynamics during cell cycle progression (hyper-fusion at the G1/S boundary, fission in mitosis), apoptosis (fission and dysfunction) and glucose starvation (reversible hyper-fusion), as well as MiDAS in response to *SIRT3* knockdown or oxidative stress. Our model also recapitulates the protective role of NAD$^+$ and external pyruvate.

---

[1] Present address: Complex Networks and Systems, Luddy School of Informatics, Computing, and Engineering, Indiana University, Bloomington, IN 47408, U.S.A.

[2] Present address: Stanford University School of Medicine, Stanford, CA 94305, U.S.A.

We offer testable predictions about the growth factor- and glucose-dependence of MiDAS and its reversibility at different stages of reactive oxygen species (ROS)-induced senescence. Our model opens the door to modeling distinct stages of DNA-damage induced senescence, the relationship between senescence and epithelial-to-mesenchymal transition in cancer and building multiscale models of tissue aging.

Keywords: MiDAS, Boolean network model, NAD^+, mitochondrial fusion/fission, mitochondrial ROS, cell cycle

Abbreviations:[3] ROS, MiDAS, NAD^+, NADH, ECT, TCA, $\Delta\Psi_M$, SASP, EMT, MOMP, SAC

Introduction

Aging is a major risk factor for cancer [1]. One culprit rendering aged tissue environments hospitable to tumor progression is the prevalence of senescent cells [2,3]. As senescence involves permanent cell cycle arrest, it was thought to be primarily tumor suppressive [4]. However, the inability of senescent cells to become cancerous themselves is counterbalanced by their effects on their neighbors. Senescent cells secrete a complex cocktail of signals termed the senescence-associated secretory phenotype (SASP), which drives proliferation, migration, and epithelial-to-mesenchymal transition (EMT) in their neighbors [4,5]. In brief localized doses, SASP can aid wound healing – as long as senescent cells are subsequently cleared by the immune system [6,7]. In contrast, chronic SASP amplified by high senescent cell density in aging tissues also causes oxidative damage and senescence-induced senescence [8]. Mixed with proliferative and EMT-promoting signals, this SASP microenvironment is favorable for chronic inflammation and cancer evolution [4,5].

An aspect of tissue aging associated with oxidative damage is mitochondrial dysfunction, which has been documented to accumulate with age in both post-mitotic cells and mitotically active tissues [9,10]. In addition to a low-efficiency electron transport chain and reduced ATP production, mitochondrial dysfunction is accompanied by low cellular and mitochondrial NAD^+/NADH ratios and increased ROS production [9]. Mitochondrial dysfunction has been shown both to trigger senescence and be a feature of senescent cells [9,11,12]. Several plausible, potentially redundant mechanisms were proposed for the former, including ROS-induced DNA damage [13] and *p53* activation by the energy sensor *AMPK* [14]. An in-depth investigation of mitochondrial dysfunction-associated senescence (MiDAS) in dividing cells revealed that a low NAD^+/NADH ratio was central as both a driver and consequence of increased mitochondrial ROS production [15]. Indeed, knocking out *SIRT3,* an NAD^+-dependent protein deacetylase that helps detoxify ROS and protect mitochondria from damage [16], resulted in MiDAS. Directly damaging mitochondria by mtDNA depletion or inhibition of the electron transport chain had a similar effect.

---

[3] ROS: reactive oxygen species; MiDAS: Mitochondrial Dysfunction-Associated Senescence; NAD: Nicotinamide Adenine Dinucleotide; NADH: nicotinamide adenine dinucleotide (NAD) + hydrogen (H); ECT: Electron Transport Chain; TCA cycle: tricarboxylic acid cycle; $\Delta\Psi_M$: mitochondrial membrane potential; SASP: Senescence-Associated Secretory Phenotype: EMT: epithelial-mesenchymal transition; MOMP: mitochondrial outer membrane permeabilization; SAC: Spindle Assembly Checkpoint

Culturing these cells in pyruvate could prevent MiDAS, presumably by boosting NAD^+-producing pyruvate-to-lactate conversion to sustain enhanced glycolysis (which needs NAD^+), and thus a proliferative Warburg effect [17]. In contrast, chemical manipulations that directly lowered NAD^+ reliably led to MiDAS, while boosting NAD^+ protected cells from senescence. What set MiDAS apart from DNA damage-induced deep senescence was its distinct SASP. High *AMPK* and sustained *p53* activation prevented these cells from producing the *NF-κB*-mediated inflammatory arm of SASP (IL-1/6/8, CXCL1/2), characteristic of irradiated cells.

A paradoxical aspect of the relationship between mitochondrial dysfunction and DNA damage-induced senescence is that, on one hand, hyperfused mitochondria with low membrane potential ($\Delta\Psi_M$) are often observed in senescence [18]. On the other hand, secreting *NF-κB*-mediated SASP requires *functional* mitochondria with low *AMPK* and *p53* [15,19,20]. A potential solution to the paradox is the observation that SASP appears late in senescence (after ~ 6 days) [21], around the time that Senescence-Associated Heterochromatin Foci are established in part by an increase in *HMGA1* [22]. This chromatin modifier was shown to induce nicotinamide phosphoribosyl-transferase (*NAMPT*) expression [19] – a rate-limiting enzyme of the NAD^+ salvage pathway responsible for most NAD^+ production in mammals [23]. This chain culminates in a reversal of mitochondrial dysfunction, increasing the translation of SASP proteins. Meanwhile, reactivation of *NF-κB* due to the downregulation of *p53* in deep senescence [24] drives mRNA expression of the pro-inflammatory SASP. The intriguing implication of this is that MiDAS may not be an inherently distinct cell fate from DNA damage-induced deep senescence. Rather, MiDAS may be an early stage that cells with intact mitochondrial DNA and protective enzymes such as *SIRT3* recover from as they deepen senescence. In contrast, cells in which MiDAS is triggered by unrepairable or ongoing mitochondrial damage (e.g., loss of mtDNA or *SIRT3*) cannot progress past the MiDAS stage and maintain a distinct, *NF-κB*-independent SASP [15].

Missing from the above description is another apparent contradiction related to the morphology of mitochondrial networks in healthy versus senescent cells. On one hand, dysfunctional mitochondria in damage-induced senescent cells are hyperfused [11,25,26]. On the other hand, hyperfusion is associated with an *increased* $\Delta\Psi_M$ and ATP generation [27], especially at the G1/S boundary of the cell cycle where it fuels *Cyclin E* activation and DNA replication (**Fig. 1A**) [28]. In line with this, *AMPK* activation by ATP shortage under starvation and/or stress ultimately promotes hyperfusion via *PGC1α*-induced mitofusin activation (**Fig. 1B**)[4] [30,31]. This is part of a negative feedback loop: hyperfusion increases ATP production and lowers *AMPK*, which in turn relieves hyperfusion by interrupting the feedback. On the opposite end of the morphology scale, the mitochondrial network fragments during mitosis without significant $\Delta\Psi_M$ loss (**Fig. 1C**) [28,32], while mitochondrial fragmentation in apoptosis aids the permeabilization of the outer membrane and crashes the $\Delta\Psi_M$ (**Fig. 1D**) [33]. None of these processes directly explain how the homeostatic fusion/fission dynamics are disrupted in senescence, or why the hyperfused network gets stuck in a dysfunctional state.

Published computational models of mitochondrial function and/or dysfunction generally address a single aspect of these quandaries [34]. One group of models focuses on ROS production [35–38] ROS propagation [39], or DNA damage-induced NAD^+ loss [40], all in the absence of mitochondrial morphological dynamics. Another group models the homeostasis of mitochondrial morphology in the absence of acute energy stress and/or increased ROS [41–43]. The two exceptions we are aware of are the Pezze et. al. model [25], the first to center mitochondrial dysfunction as a driver of damage-induced senescence and the original inspiration of this study. The other model by Hoffman et. al., while specific to *C. elegans*, contains a key feedback loop between NAD^+ generation by functional mitochondria and NAD^+-mediated sirtuin activation and antioxidant gene transcription [44]. This feedback has a similar role to that of NAD^+ in *SIRT3*-mediated protection from mitochondrial ROS [15].

---

[4] In addition, *AMPK* is also part of an incoherent feed-forward loop (Fig. 1B), such that its *immediate* effect on mitochondria is fragmentation [29], subsequently reversed by *AMPK*-induced *p53* [18].

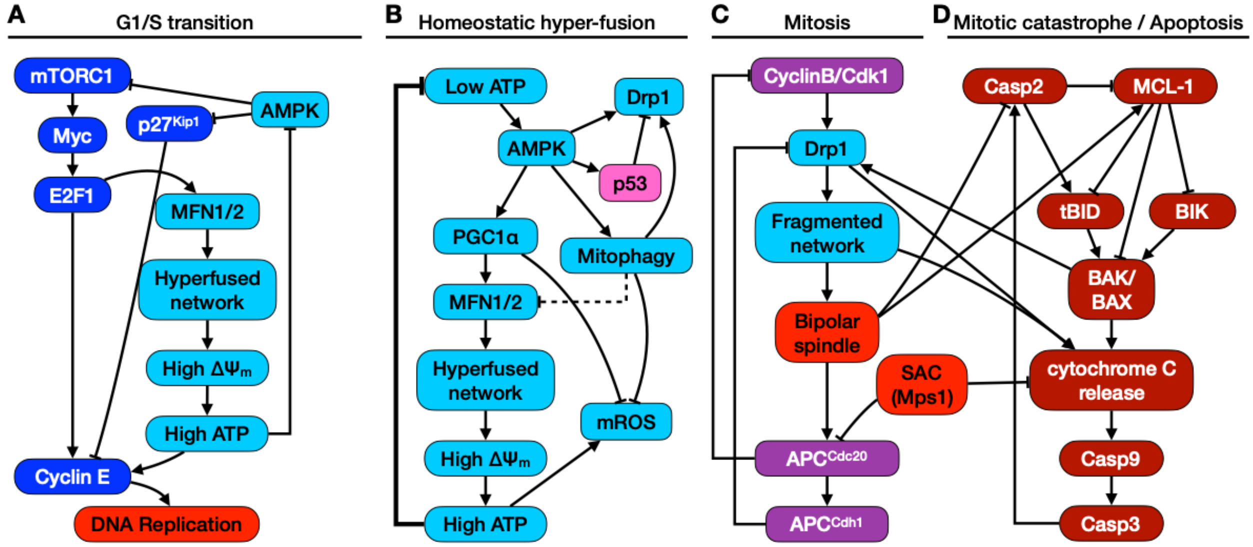
A
G1/S transition
mTORC1
Myc
p27Kip1
AMPK
E2F1
MFN1/2
Hyperfused network
High ΔΨm
High ATP
Cyclin E
DNA Replication
B
Homeostatic hyper-fusion
Low ATP
Drp1
AMPK
p53
PGC1α
Mitophagy
MFN1/2
Hyperfused network
mROS
High ΔΨm
High ATP
C
Mitosis
CyclinB/Cdk1
Drp1
Fragmented network
Bipolar spindle
SAC (Mps1)
APCCdc20
APCCdh1
D
Mitotic catastrophe / Apoptosis
Casp2
MCL-1
tBID
BIK
BAK/ BAX
cytochrome C release
Casp9
Casp3

Figure 1. Control of mitochondrial morphology by cell cycle, energy stress and apoptosis. A) At the G1/S boundary, *E2F1* induces microfusin (*MFN2*) to generate a hyperfused mitochondrial network that can supply the increased ATP demands of DNA synthesis. **B)** A drop in the ATP/AMP ratio activates *AMPK*, which rapidly fragments the mitochondrial network by activating *Drp1*, but ultimately results in transcriptional *Drp1* repression and *MFN1/2* upregulation via *p53* and *PGC1α*, respectively. The resulting hyperfused network restores ATP, closing a homeostatic negative feedback loop. While increased ATP generation also increases mitochondrial ROS, both *PGC1α*'s target genes and *AMPK*-induced mitophagy work to counteract it. **C)** At the start of mitosis, *Cdk1* activates *Drp1* to trigger fission, which is required for proper spindle formation and Spindle Assembly Checkpoint (SAC) passage. APC^{Cdh1} then lowers *Drp1* levels in anaphase. **D)** During mitotic catastrophe, failure to assemble a bipolar spindle and pass SAC activates *Caspase 2,* which in turn truncates BID to trigger apoptosis. BAK/BAX recruit *Drp1* to mitochondria to fragment them, aiding *Cytochrome C* release and downstream executioner caspase activation. References for each link in **SM Table 1.**

Here we offer a mechanistic regulatory network model that brings together mitochondrial energy production and its failure, leading to MiDAS involving dynamic changes in mitochondrial morphology. To do this, we focus on the interdependence of mitochondrial morphology, renewal by mitophagy, and ROS generation. Namely, hyperfused mitochondria are protected from mitophagy [45], but also generate more ROS [46]. Thus, the hyperfused state must be either short-lived or well-protected from ROS through scavenging that requires *SIRT3*. Otherwise, mitochondria exhaust their undamaged components and diminish their ATP production [12]. We hypothesize that when mitochondrial ROS increases and NAD^+ levels drop due to ETC damage, this system can lock itself into MiDAS via the following positive feedback: the hyperfused network no longer restores ATP, *AMPK* sustains hyperfusion, which in turn continues to produce

ROS unprotected by *SIRT3* due to low NAD$^+$ – further compromising ATP production. Leveraging this hypothesis and key insights from the Pezze et. al. model of mitochondrial dysfunction in senescence [25], we propose a regulatory network model which integrates the role of NAD$^+$ in preventing MiDAS stabilization. We combine this novel mechanism with previously a published model of cell cycle regulation [47] into a mechanistic model which synthesizes and reproduces the connection between mitochondrial dynamics and cell cycle progression, apoptosis, glucose starvation and finally, *SIRT3* deletion- or ROS-driven MiDAS along with its rescue by external pyruvate. We then use this model to generate testable predictions about MiDAS in healthy versus cancer-related mutant cells.

Computational Methods

I. Model and code availability. **a)** The Boolean model presented here was deposited in the BioModels online repository (MODEL2312140001) and will be available following publication. Biological justification for all model components, along with model files in a variety of formats, are included in **SM Files 1-3** (*.dmms* format read by *dynmod*, *.BooleanNet* format read by the BooleanNet Python library [48], *.gml* format for editable network visualization read by yED [49]). **c)** All original code is available on GitHub (*https://github.com/Ravasz-Regan-Group*). These include the Haskell code package *dynmod* used to parse *.dmms* model files, visualize attractors in the model's combinatorial environment space, run and visualize time courses, export the network's 2D layout, and render the LaTeX-formatted supplementary file containing the model's biological justification. The *dynmod* parser generates files read by a C++ XCode package called *Boolean_code_for_MiDAS* that runs all statistics on the rate of cell cycle progression, cell cycle errors, apoptosis and MiDAS. Instructions to reproduce all figures are detailed below and included with each code packet (**SM Files 4-12**). Additional information to run the simulations reported here is available upon request from E.R.R.

II. Boolean model building. To build the Boolean model we extended our previously published cell cycle and apoptosis network [47] with pathways that control glycolysis, mitochondrial ATP production, mitochondrial morphology, and DNA damage response (a bare-bones circuit focused on *p53/p21*-mediated cell cycle arrest). The model synthesizes qualitative experimental data from 466 papers into a 134-node Boolean network in which all links and regulatory functions are experimentally justified (**SM Table 1**; *black*: published in [47]; *gray:* changes from [47] included in [50,51]; *blue*: new nodes/links). For details of our model construction approach, the use of synchronous vs. asynchronous update, automatic module isolation from the larger network, storing our model in *Dynamically Modular Model Specification* (*.dmms*) format (**SM File 1**), as well as using *dynmod* for all functionality except visualizing attractors in 5D and running simulations, see STAR Methods in [50]. Key command-line tags described in [50] include: **-t --coord_colors** (output *.BooleanNet* [**SM File 2**] and files *Boolean_code_for_MiDAS* uses to run statistics); **-g** (*.glm* format, **SM File 3**), **-u** (update coordinates from user-organized *.gml* into *.dmms*), and **-s** (generate formatted LaTeX document and bibliography for **SM Table S1**). For editing *.dmms* files on Mac OX / Windows, we recommend *BBEdit* / *Notepad++* with DMMS language modules included as **SM File 4** (copy to *~/Library/Application Support/BBEdit/ Language Modules*) and **SM File 5** (import under the *Language/User Defined Language* tab).

III. Sampling the model's state space to map its synchronous attractors. We used synchronous Boolean modeling to find every stable phenotype and/or oscillation (attractor) of the model using a stochastic sampling procedure [52] implemented in *dynmod* and *Boolean_code_for_MiDAS* [53,47,51,50]. For an exhaustive search, we ran

```
dynmod --grid '20 10 0.02 10' MiDAS_Cell_Cycle_Arrests_Apoptosis.dmms
```

to generate a 20 x 10 grid of independent sampling attempts (see [50]). Once this is finished, *dymod* runs a time course from each attractor by changing one environmental variable at a time to increase its ability to detect low-stability states in environments where most of the state space is occupied by large basins. Its final outputs are a heat-map of the number of attractors in each sampling run (verifying that most independent sampling runs find all 96 attractors; not shown), and all attractors collated into a single *.csv* (**SM File 6**).

IV. Time series with non-saturating inputs and partial knockdown / hyper-activation. The current version of *dynmod* parses a user-generated experiment file to run simulations (*.vex* format). For editing *.vex* files on Mac OX / Windows, we recommend *BBEdit* / *Notepad++* with VEX language modules included as **SM Files 7, 5**. Precise use of each command is described in *MiDAS__Main_Figures.vex* (**SM File 8**) and *MiDAS__SM_Figures.vex* (**SM File 9**), helping readers reproduce *dynmod*-generated figures and documenting the use of *.vex* commands. To run these, use the **-e** tag:

```
dynmod -e MiDAS__Main_Figures.vex MiDAS_Cell_Cycle_Arrests_Apoptosis.dmms
dynmod -e MiDAS__SM_Figures.vex MiDAS_Cell_Cycle_Arrests_Apoptosis.dmms
```

Key *.vex* command blocks include:

— *Sampling:* new sampling and/or use of previously generated attractors *.csv* files, with options to only sample a subspace of the model's full environment space and expand iteratively.

— *InputSpaceDiagram:* visualization of all attractors represented as barcodes that represent phenotype-combinations of relevant modules (specified in the model *.dmms* file, *SwitchProfiles*).

— *Pulse1:* synchronous time course from a subset of cell states in a given initial environment, exposed to a reversible change in a single environmental signal.

— *GeneralExperiment:* synchronous or asynchronous time course from a subset of cell states in a given initial environment, exposed to an arbitrary sequence of manipulations defined in distinct time windows. Within each window the cell's external environment may be set to an arbitrary non-saturating value-combination (e.g., *GF_High* = 0.5 & *Glucose* = 0.3). In addition, a subset of internal nodes can be partially / fully knocked down / hyperactivated. To simulate non-saturating inputs, *dynmod* overrides their value with a stochastic ON/OFF sequence with a fixed probability, tuning the cell's average exposure. Similarly, partial knockdown/ hyperactivation of a node involves forcing it OFF/ON with a fixed probability in each time-step; otherwise allowing it to obey its Boolean rule [53,47,51,50] (justification / limitations of approach detailed in [48]).

To reproduce the synchronous time courses described in the model's predecessor in [47], use *MiDAS__Sizek_Results.vex* (**SM File 10**):

```
dynmod -e MiDAS__Sizek_Results.vex MiDAS_Cell_Cycle_Arrests_Apoptosis.dmms
```

V. Phenotype statistics in non-saturating stochastic environments. All phenotype statistics were generated by *Boolean_code_for_MiDAS*via the *in silico* experiments listed and annotated in *VirtualExp_run_stats.txt* (**SM File 11**), using *VirtualExp_Phenotypes_for_STATS.txt* (**SM File 12**) to specify phenotypic signatures of interest (*Boolean_code_for_MiDAS's* attractor sampling and phenotype statistics algorithms are detailed in [48]). Once the statistics are written to disk, *Boolean_code_for_MiDAS* generates Python code and pdfs to show the results as stacked bar graphs. Sampling commands used here include: *NonSaturating_Stats_Scan_1Env_fnKDOE* (generates either a figure panel with bar graphs of all phenotype statistics at increasing values of a single input from 0% to 100% (*x* axis), or a *series* of panels where the *x* axes are increasing levels of a node's knockdown/hyper-activation, while the series show results at increasing values of a single input from 0.05% to 95%); *Phenotype_Change_in_Mutants_Across_Phase_Space* (generates a panel of heat-maps for each phenotype, showing its prevalence in wild-type vs. mutant cells across all combinations of three environments set to 0, 0.05, 0.5 and 0.95).

VI. Previously introduced regulatory modules. Detailed descriptions of *Growth factor signaling*, *Replication origin licensing*, *Restriction switch*, *Mitotic phase switch*, *Apoptotic switch* and *Cell cycle processes* are detailed in [47,53].

Results

1. Extending a Mitogen Signaling-Driven Cell Cycle and Apoptosis Model to Account for the Regulation of Mitochondrial Morphology

To examine the way MiDAS arises from the dynamics of the regulatory processes that govern mitochondrial energy production and the dynamics of fusion and fission, we used our previously published model of growth signaling, cell cycle, and apoptosis as a starting point [47]. This Boolean regulatory network model was shown to reproduce *PI3K* oscillations linked to cell cycle progression, capture the cell cycle-phase dependent roles of *Plk1*, and reproduce cell cycle errors in perturbed cells (e.g., hyperactive *PI3K,* loss of *FoxO1/3* or *Plk1*) such as mitotic catastrophe, aneuploidy, and endoreduplication. Here we extend this model to include three new regulatory modules, capturing changes in metabolism, DNA damage signaling, and a mitochondrial module capturing energy production linked to the dynamics of mitochondrial morphology.

First, the ***Warburg*** module accounts for glycolysis and the Warburg effect – the increase in glucose uptake and lactate production characteristic of dividing cells (**Fig. 2A**). The module focuses on the regulatory logic behind the shift from moderate glycolysis producing pyruvate for the TCA cycle to increased glycolysis (*Glycolysis_H* node) coupled with fermentation (pyruvate to lactate conversion) [17]. *HIF-1α*-mediated fermentation can support ATP production in the absence of oxidative phosphorylation, but its other critical function is to regenerate the cytosolic pool of NAD^+ (*NADp_c* node) required for and depleted by glycolysis (**Fig. 2A**; *Glycolysis_H* ⊣ *NADp_c*; overridden by *Fermentation* → *NADp_c*). The shift is induced by *HIF-1α* and/or *Myc*-mediated up-regulation of glucose transporters and glycolytic enzymes; blocked by *p53* [54].

Second, the ***DNA Damage Signaling*** module is a representation of ROS-mediated *p53* and *p21* activation (**Fig. 2B**) [55]. The rules for *p53* activation include phosphorylation by *AMPK*, *ATM* and *ATR* [14,56], as well as its lack of response in mitosis (in the absence of a nuclear membrane, *p53* is captured at the centrosomes and remains transcriptionally inactive [57]). Some of *p53*'s effects, such as *Cyclin B* repression, only occur after sustained *p53* activity (or repeated *p53* oscillations) [58,59]. We account for this via four nodes that track increasing/sustained *p53* activity under ongoing damage, and only link the 4th level (*p53_4* node) to these targets. In contrast, the effect of *p53* on metabolic and cell cycle targets (*HIF1α, Myc, FoxO1/3, p21*) are immediate [60].

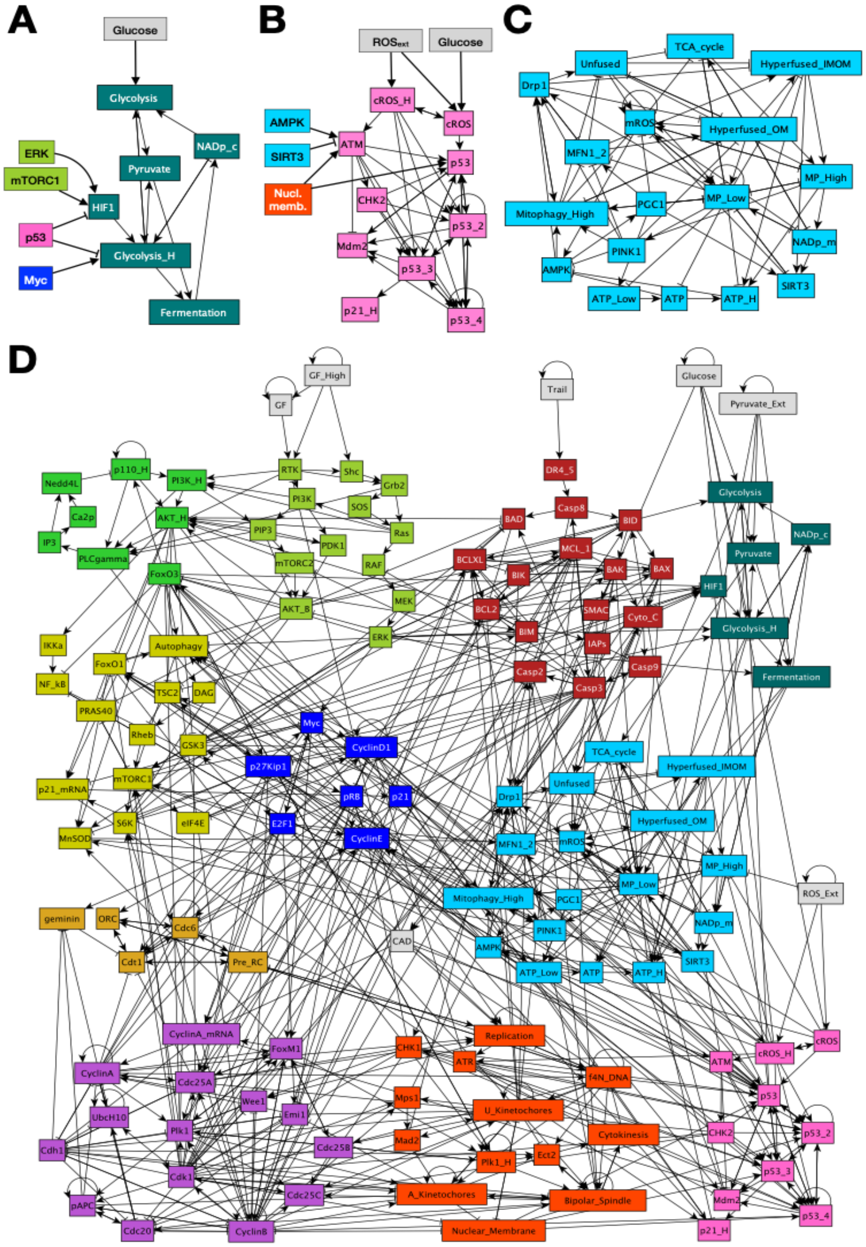
A
Glucose
Glycolysis
ERK
mTORC1
Pyruvate
NADp_c
HIF1
p53
Glycolysis_H
Myc
Fermentation
B
ROSext
Glucose
cROS_H
AMPK
cROS
ATM
SIRT3
p53
Nucl. memb.
CHK2
p53_2
Mdm2
p53_3
p21_H
p53_4
C
TCA_cycle
Unfused
Hyperfused_IMOM
Drp1
mROS
Hyperfused_OM
MFN1_2
MP_High
PGC1
MP_Low
Mitophagy_High
NADp_m
PINK1
AMPK
SIRT3
ATP_Low
ATP
ATP_H
D
GF_High
GF
Trail
Glucose
Pyruvate_Ext
p110_H
Nedd4L
PI3K_H
RTK
Shc
Grb2
DR4_5
PI3K
SOS
Ca2p
AKT_H
PIP3
Casp8
BAD
BID
Glycolysis
NADp_c
IP3
PLCgamma
PDK1
Ras
MCL_1
Pyruvate
FoxO3
mTORC2
RAF
BCLXL
BIK
BAK
BAX
HIF1
AKT_B
MEK
BCL2
SMAC
Cyto_C
Glycolysis_H
IKKa
Autophagy
ERK
BIM
IAPs
NF_kB
FoxO1
Casp2
Casp9
Fermentation
TSC2
DAG
Casp3
PRAS40
Myc
Rheb
GSK3
CyclinD1
TCA_cycle
Hyperfused_IMOM
p27Kip1
p21_mRNA
mTORC1
pRB
p21
Drp1
Unfused
S6K
eIF4E
E2F1
Hyperfused_OM
MnSOD
CyclinE
MFN1_2
mROS
MP_High
MP_Low
Mitophagy_High
PGC1
ROS_Ext
geminin
ORC
Cdc6
PINK1
NADp_m
CAD
AMPK
SIRT3
Cdt1
Pre_RC
ATP_Low
ATP
ATP_H
CyclinA_mRNA
Replication
FoxM1
CHK1
cROS
ATR
ATM
cROS_H
CyclinA
4N_DNA
Cdc25A
p53
Wee1
Mps1
UbcH10
Emi1
U_Kinetochores
Plk1
Cdh1
Cdc25B
Mad2
Cytokinesis
CHK2
p53_2
Plk1_H
Ect2
Cdk1
p53_3
Cdc25C
A_Kinetochores
Bipolar_Spindle
Mdm2
pAPC
p53_4
Cdc20
CyclinB
Nuclear_Membrane
p21_H

Figure 2. Boolean regulatory network model of cell cycle-linked mitochondrial energy production and shape dynamics. A) Warburg effect module tracking NAD$^+$ use and regeneration by glycolysis and fermentation, with key influences from cell cycle control (*ERK*, *mTROC1*, *Myc*) and *p53*. **B)** DNA damage module showing ROS or *ATM/Chk2*-mediated *p53* activation, its 4-node persistence tracker, negative feedback via *Mdm2*, downstream *p21* induction, and key influences from the mitochondrial module (*AMPK*, *SIRT3*) and mitosis. **C)** Mitochondrial regulatory switch controlling energy production, mitochondrial NAD$^+$ homeostasis, morphology, and ROS production. **D)** Modular network representation of our Boolean model. *Gray:* inputs representing environmental factors; *green*: Growth Signaling (*lime green*: basal AKT & MAPK, *bright green:* PI3K/AKT oscillations, *mustard*: *NF-κB* & autophagy (new), *mTORC1*, *GSK3*, *FoxO1*); *dark red:* Apoptotic Switch; *light brown:* Origin of Replication Licensing; *blue:* Restriction Switch; *purple:* Phase Switch; *dark orange:* cell cycle processes; *dark green:* Warburg effect; *teal:* mitochondrial switch; *pink*: DNA damage response; → : activation; ⊣ : inhibition.

Third, the ***Mitochondria*** module contains a detailed map of all the relevant interactions that govern mitochondrial energy production coupled to the dynamics of their morphology (**Fig. 2C**) [61]. Briefly, the TCA cycle uses (and requires) pyruvate and mitochondrial NAD$^+$, to generate NADH. The electron transport chain (ETC) utilizes the high energy electrons of NADH and regenerates NAD$^+$ while generating the mitochondrial membrane potential ($\Delta\Psi_M$). Thus, through feeding the ETC the TCA cycle helps maintain normal mitochondrial membrane potential ($\Delta\Psi_M$), which is utilized by ATP synthase to synthesize ATP, and keep *AMPK* inactive. To capture the four qualitatively different regimes of ATP/AMP ratio in cells (deadly, survivable but with activated AMPK, normal, and high), we use three Boolean nodes for ATP (bottom row on **Fig. 2C**). Upon *AMPK* activation, the module captures the increase in mitophagy (*Mitophagy_High* node) as well as *PGC1α* activation leading to increased mitochondrial biogenesis, ROS reduction, and increased transcription of the mitofusins *MFN1/2,* which start mitochondrial fusion at the outer membrane (*Hyperfused_OM* node) [62]. In mitochondria with normal $\Delta\Psi_M$, the inner membranes also fuse (*Hyperfused_IMOM* node) to increase ATP production and lower *AMPK*. This negative feedback is homeostatic; hyperfusion only persists as long as ATP is in demand. Here, *SIRT3* is a critical protector of $\Delta\Psi_M$ as it lowers mitochondrial ROS and protects its ATP-generating potential [16]. In contrast, activation of the fission protein *Drp1* results in a highly fragmented network seen in mitotic or apoptotic cells [32,63]. The mitochondrial module interacts with cell cycle control and apoptosis as summarized in **Fig. 1**. The complete regulatory network is shown on **Fig. 1D**, with detailed node and link justifications described in **SM Table 1** (2D layout in **SM File 3**; *gml* format).

2. Extended Model Reproduces Known Cell Cycle-Dependence of Mitochondrial Morphology as Well as G1 Arrest with Mitochondrial Fusion in Glucose-Starved Cells

The principal predictive feature – and means of validation – of Boolean models is the equilibrium dynamics emergent from the network's logical regulatory rules [64]. All Boolean models have a set of steady states and/or limit cycles, also referred to as attractors. Every dynamically evolving system eventually converges into one of these states (or sets of states) and, unperturbed, will stay there indefinitely. The canonical expectation is that the attractors of biological Boolean models represent biologically meaningful phenotypes [65]. The first step in model validation is examining the qualitative match between the steady states of a Boolean model and the expected phenotypes. We expect that both changes in the model cell's environmental inputs and perturbations of its internal nodes result in biologically meaningful signal transduction and phenotype transitions, in accordance with experimental data. Thus, our first goal is to validate our extended model by comparing its dynamical states and responses to the experimental literature. In the *in silico* simulation results discussed below we use synchronous update (all nodes are updated simultaneously in each time-step) and thus the results are deterministic. This allows us to examine the effects of precisely timed perturbations, which are especially relevant in triggering responses known to change with cell cycle progression.

As expected, our extended model has a quiescent attractor in the presence of limited mitogens, similar to its predecessor model [47]. Metabolically, this state is characterized by moderate glycolysis and pyruvate flux to the TCA cycle, normal $\Delta\Psi_M$, and nominal relative ATP as well as mitochondrial NAD^+ (**Fig. 3A, SM Fig 1A,** *left*). Upon mitogen stimulation the model mimics cell cycle entry (**Fig. 3A,** *middle*), then cell cycle-exit upon a drop in mitogens to survival-sustaining levels (**Fig. 3A,** *middle*). In addition to reproducing the experimentally observed behaviors captured by the original Sizek et. al. model (**Table 1**, *gray font;* **SM File 11**) [47], our new model further captures the cell cycle-dependent dynamics of mitochondrial morphology (**Table 1A**, *black font*). These include mitochondrial hyperfusion at the G1/S transition (**Fig. 3A,** *red box & arrow, left*) [28], reset to a G0-like morphology in G2, and an unfused (fragmented) state in mitosis (**Fig. 3A,** *red box & arrow, right*) [32]. Note the enhanced protective *SIRT3* activity during the reversible G1/S hyperfusion, predicted by the model as a requirement for keeping the hyperfused network healthy (*left-side red box / arrow*).

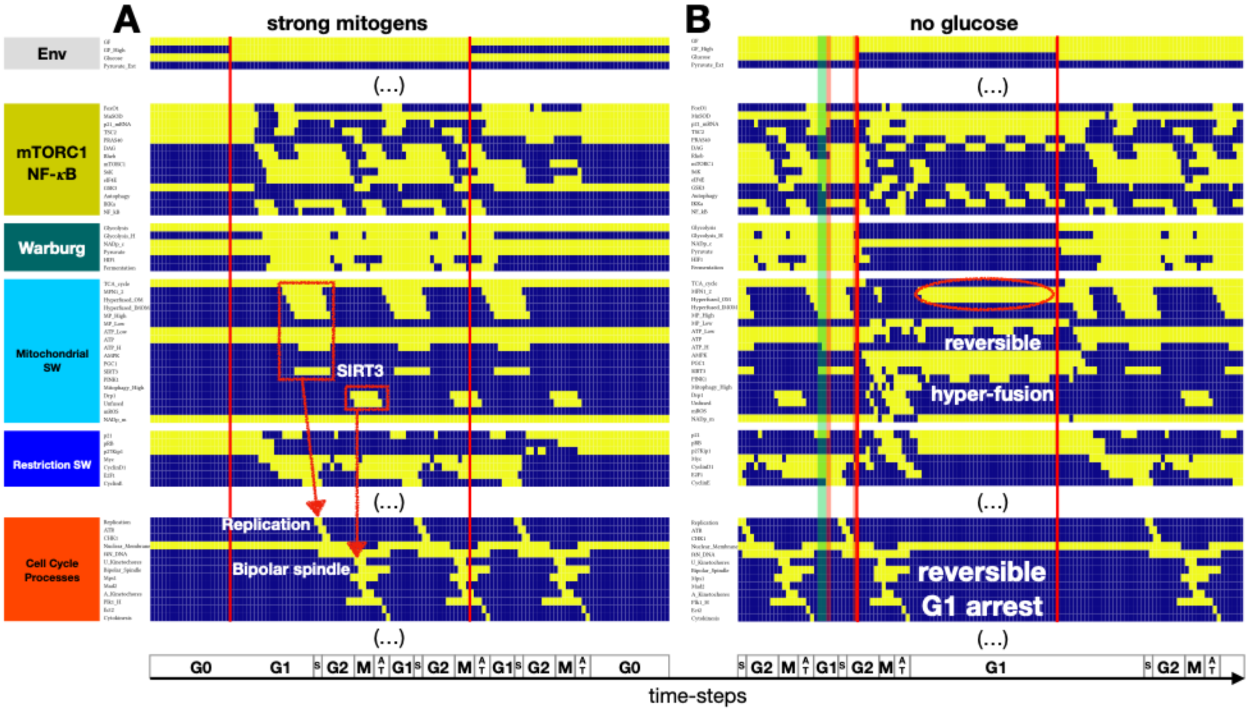

Figure 3. Model reproduces cell cycle-linked mitochondrial dynamics (hyperfusion at G1/S, fission in mitosis) and G1 arrest in response to glucose withdrawal. A) Dynamics of relevant regulatory molecule expression/activity during exposure of a quiescent cell to a saturating mitogenic signal (full network dynamics in **SM Fig. 1A**). **B)** Dynamics of relevant regulatory molecule expression/activity in a dividing cell responding to glucose withdrawal in early G1 (full network dynamics in **SM Fig. 1B**). *X-axis:* time-steps annotated by cell cycle phase (*G0*: quiescence; *G1*: start of cell cycle entry; *S*: DNA synthesis; *G2*: growth phase 2; *M*: metaphase; *A T*: anaphase, telophase, cytokinesis); *y-axis:* nodes organized by regulatory modules; *yellow/dark blue:* ON/OFF; *vertical red lines:* start/end of signal; *red boxes with arrows:* morphological changes to mitochondria linked to cell cycle processes; *red oval*: reversibly hyperfused mitochondrial network; *shaded green band:* window of glucose withdrawal resulting in endoreduplicaiton (**SM Fig. 6A**); *shaded red bands:* windows of glucose withdrawal resulting in apoptosis (**SM Fig. 6B-C**).

We next validated our model against known cell cycle perturbations. These include: a) fragmentation of the mitochondrial network during apoptosis triggered by *Trail* or mitotic catastrophe triggered by *Plk1* loss [66,67] (**SM Fig. 2**); b) G1 arrest in cells that cannot form hyperfused mitochondria with high $\Delta\Psi_M$ in late G1 due to *MFN2* knockdown [68] or reduced $\Delta\Psi_M$ [28] (**Table 1B & SM Fig. 3**); c) reduced mitotic fission and reduced proliferation in cells expressing dominant negative *Drp1* [28,32] (**Table 1B**, **SM Figs. 4, 5**); d) apoptosis in cells with prolonged exposure to the *Drp1 inhibitor* mdivi-1 (**SM Figs. 4, 5**, predicted here to involve mitotic catastrophe) [28]; d) severe metaphase chromosome misalignment and apoptosis in cells treated with high doses of a mitochondrial hyperfusion inducer [28,69] (**SM Fig. 4C**).

Another physiological signal with a reversible effect on mitochondrial morphology is non-lethal glucose starvation, shown to induce a reversible G1 arrest [70]. This cell state is characterized by strong *AMPK* activation, increased mitochondrial fusion and decreased mitophagy [45]. Our model reproduces these observations, including a reversible G1 arrest accompanied by *AMPK*-driven *PGC1α*-activation, increased *MFN1/2* expression mitochondrial hyperfusion, and delayed cell cycle entry upon re-exposure to glucose (**Table 1C**; **Fig. 3B, SM Fig 1B**). Based on the molecular mechanisms driving our model's dynamics, we predict that these mitochondrial networks mainly fuse their outer membranes (*Hyperfused_OM* = ON; *Hyperfused_IMOM* = OFF), as inner membrane fusion (executed by *OPA1*) requires normal $\Delta\Psi_M$ [71]. Moreover, we do not expect a drastic drop in mitochondrial (or cytosolic) NAD$^+$, as both primary processes consuming NAD$^+$ (TCA cycle and glycolysis), are paused alongside reduced NAD$^+$ generation by the ETC.

As long as glucose withdrawal in our model occurs in late G2 or mitosis, we observe a G1 arrest (**Fig. 3B,** *non-shaded areas*). Outside this window, however, we predict two alternative cell fates (**Table 1C**, *blue font*; **SM Fig. 6**). First, we predict G2 arrest followed by endo-reduplication in a subset of cells that experience glucose withdrawal in a pre-committed G1 state; one that passed the restriction point *before* finishing its previous cytokinesis [72] (**SM Fig. 6A**). Our predicted mechanism involves *p53*-mediated *Myc* repression downstream of ROS accumulation, which decreases *FoxM1* levels and results in a failure to establish a self-sustaining G2 state (positive feedback on **SM Fig. 6A**) [73–75]. Upon re-exposure to glucose, the cell starts another round of DNA replication (**SM Fig. 6A**, *bottom red circle*). Second, we predict that glucose withdrawal-induced mitochondrial hyperfusion that persists into mitosis can delay mitotic mitochondrial fragmentation long enough to cause spindle assembly defects and mitotic catastrophe (**SM Fig. 6B,C**).

Table 1. Model reproduces experimentally observed mitochondrial dynamics during cell cycle, perturbations to mitochondrial fusion/fission proteins, and glucose starvation.

Model behavior ✤ new here / * inherited from [47] / ✻ prediction	**Figure**	**Experimentally observed cell behavior**
A. Mitochondrial dynamics during cell cycle progression		
• Stimulation with low mitogens (*GF* = ON but GF_{High} = OFF) leads to quiescent cells (**Fig 3A**, *left*). • Stimulation with GF_{High} = ON leads to continuous cell cycle progression (**Fig 3A**, *middle*).	**Fig 3A**	– An increasing fraction of cells enter the cell cycle at increasing *EGF* or serum concentrations, reaching ~100% at 20 ng/mL *EGF* / 5% serum in MCF10A cells [76]; similar results were reported for rat embryonic fibroblasts [77]. – Mouse fetal fibroblasts display wide heterogeneity in the timing of the G1 / S transition regardless of the level or duration *of IGF-I, EGF, PDGF-AA*, or *PDGF-BB* treatment [78].
• Mitogen washout experiments (GF_{High} = ON to GF_{High} = OFF) show that a cell can pre-commit to another division cycle before finishing its current mitosis and execute a full cell cycle in the absence of mitogenic stimulation (**Fig 3A**, *right*).	**Fig 3A**	– Rapidly dividing mammalian cells (MCF10A, Swiss3T3) can pre-commit to a division cycle before finishing their current one; they often execute a full cell cycle after mitogen withdrawal, such that their last exposure to mitogens occurs sometime during the previous G2 phase [72].

✣ Stimulation with GF_{High} = ON leads to cyclic mitochondrial dynamics during cell cycle progression (**Fig 3A**, *middle*), involving: ✣*E2F1*-induced hyperfusion of the mitochondrial network at the G1/S transition, leading to increased $\Delta\Psi_M$ and ATP generation, which helps activate *Cyclin E* ∗Strong ETC activity in a healthy hyper fused network increases SIRT3 activity to block runaway ROS production. ✣Resetting of the mitochondrial network to its basal state in G2 (similar to G0) due to *E2F1* inhibition by *Cyclin A/Cdk2.* ✣*Cyclin B/Cdk1*-mediated activation of the fission protein *Drp1*, resulting in an unfused (fragmented) state with relatively normal $\Delta\Psi_M$, which aids bipolar mitotic spindle formation and SAC passage.	**Fig 3A**	– *E2F1* is a direct transcriptional inducer of *MFN2,* which in turn increases mitochondrial fusion [28]. – Mitochondrial inner membrane fusion raises the efficiency of OXPHOS and increases the network's $\Delta\Psi_M$ [27]. – A high $\Delta\Psi_M$ mediated by hyper fusion and resulting in increased ATP production in late G1 are required for *Cyclin E* accumulation and S-phase entry [28]. – *Indirect support:* SIRT3 is necessary for healthy proliferation [15]. – During mitosis, *Drp1* is phosphorylated and activated by *Cdk1/Cyclin B*, resulting in mitochondrial fragmentation and proper bipolar spindle formation [28,32,79]. – TCA cycle metabolite levels oscillate during cell cycle progression to support high $\Delta\Psi_M$ at the G1/S boundary, but do not crash in mitosis [80].
B. Perturbations of cell cycle progression accompanied by mitochondrial morphology change		
• Cycling cells experiencing *Plk1* knockdown at different points along the cell cycle, leading to: — G2 arrest when *Plk1* is lost before the G2/M transition — mitotic catastrophe when *Plk1* is lost in early metaphase — aneuploidy when *Plk1* is lost in late metaphase — no cytokinesis followed by endoreduplication when *Plk1* is lost after SAC passage.	**SM Fig. 2**	– *Plk1* activation by *Cyclin A/Cdk2* at the G2/M boundary is required for mitotic entry [81]. – *Plk1* is required for the formation and maintenance of microtubule-kinetochore attachments [82,83]. – Aneuploidy and genome duplication have been documented in *Plk1*-inhibited cells [84]. – Due to *Plk1*'s role in driving contractile ring assembly, *Plk1* knockdown in telophase blocks cytokinesis [85].
• Saturating *Trail* exposure kills quiescent as well as cycling cells. • Non-saturating *Trail* leads to fractional killing • Cells with prolonged metaphase are the most sensitive to *Trail*- mediated apoptosis.	virtual experiment in **SM File 10**	– Saturating *Trail* can kill ~100% of cells (immortalized human T lymphocytes [86], MCF10A [87], pancreatic cancer [88], glioblastoma & colon cancer cell lines [89]). – *Trail* is synergistic with microtubule-targeting chemotherapy agents that trap cells in metaphase and delay SAC [89].

✣ *Trail*-induced apoptosis leads to *BAK/BAX*-mediated *Drp1* activation, mitochondrial fragmentation, and *Cytochrome C* release, along with the loss $\Delta\Psi_M$ and increased mROS. ✻ Partial Mitochondrial Outer Membrane Permeabilization (MOMP) via initially sub-lethal *Trail* can disrupt mitochondrial dynamics in G2/M, leading to mitotic catastrophe (discussed in *Results - 3*).	**SM Fig. 10B**	– *Trail* induces *Drp1*-dependent mitochondrial fission by inducing Ser616 phosphorylation of *Drp1*, $\Delta\Psi_M$ loss, mROS, and cytochrome C release [66]. – *Indirect support*: non-lethal MOMP that only occurs in a small subset of mitochondria (minority MOMP) was documented in senescence, though it is unclear if it could be causal [90].
✣ *Caspase 2*-mediated *BAK/BAX* activation during mitotic catastrophe activates *Drp1* to induce mitochondrial fragmentation, lowers $\Delta\Psi_M$, and increases mitochondrial ROS. ✣ In contrast to fragmentation in mitosis, apoptotic fragmented mitochondria aid *Cytochrome C* release and apoptosis.	**SM Fig. 2B**	– Mitotic catastrophe in IR-treated cells requires *Drp1*-induced mitochondrial fission [91].
✣ Cycling cells experiencing *MFN1/2* knockdown show G1 arrest. ✣ Cycling cells experiencing forced low $\Delta\Psi_M$ (forced *MP_low* = ON) starting in late S-phase results in G1 arrest with no *Cyclin E* as well as increased *p21* and *p53.*	**SM Fig. 3**	– Cells infected with *Mfn2* shRNA show inhibited cell proliferation [68]. – Dividing cells treated with an oxidative phosphorylation uncoupler undergo G1 arrest, show a lack of *Cyclin E* accumulation and increased *p21* expression [28]. – Reducing $\Delta\Psi_M$ with FCCP results in G1–S arrest [28].
✣ Cycling cells experiencing partial (60%) *Drp1* knockdown cannot sustain mitochondrial fragmentation during mitosis, resulting in problems with spindle assembly and prolonged SAC arrest. ✻ Cycling cells experiencing full *Drp1* knockdown arrest at the SAC long enough to undergo apoptosis. ✣ Cycling cells experiencing a brief period of *Drp1* knockdown in G2 do not arrest their cell cycle. ✣✻ Cycling cells experiencing prolonged *Drp1* knockdown arrest at the SAC and eventually undergo apoptosis. ✣ Cycling cells experiencing 50% forced outer membrane hyperfusion show prolonged SAC arrest due to spindle assembly delays and stochastically undergo apoptosis.	**SM Fig. 4** **SM Fig. 5**	– Cells expressing dominant negative mutant *Drp1K38A* (DRP1m) fail to undergo mitochondrial fission during mitosis [32]. – *Indirect support*: high concentrations of mdivi-1 (mitochondrial division inhibitor) induce apoptosis [69]. – Cells overexpressing dominant negative *DRP1m* in a *brief* window before cells undergo mitosis experience no cell cycle inhibition [28]. – Perpetually hyperfused mitochondria generated by *prolonged DRP1m* expression significantly decreases proliferation [28]. – Cells treated with a mitochondrial division inhibitor (mdivi-1) to induce hyperfusion have severely misaligned metaphase chromosomes [28].

		– High concentrations of mdivi-1 not only block proliferation but also induce apoptosis [69].
C. Mitochondrial dynamics during glucose starvation		
✣ Cycling cells glucose withdrawal undergo reversible G1 arrest, activate AMPK, which leads to PGC1α-mediated *MFN1/2* up-regulation and indirect *Drp1* inhibition mediated by *p53* (itself induced by AMPK and increased cellular ROS production). ✣ *MFN1/2* up-regulation and *Drp1* inactivation in response to glucose withdrawal leads to reversible mitochondrial hyperfusion and no increase in mitophagy (in spite of low $\Delta\Psi_M$ due to lack of glucose). ✳ Hyperfused networks in glucose-starved cells fuse their outer membranes only, as inner membrane fusion requires normal $\Delta\Psi_M$.	**Fig. 3B**	– Non-lethal glucose starvation induces reversible G1 arrest [70] with strong *AMPK* activation [45]. – Nutrient depletion, including glucose starvation, leads to significantly elongated and interconnected mitochondria, mediated by down-regulation of *Drp1* and unopposed mitochondrial fusion [45]. – Mitochondrial hyperfusion upon nutrient deprivation protects mitochondria from mitophagy [45].
✳ Cells that experience glucose withdrawal in a pre-committed G1 state; one that passed the restriction point *before* finishing its previous cytokinesis, undergo G2 arrest followed by endo-reduplication. Predicted mechanism (positive feedback on **SM Fig. 6B**; regulatory link details in **SM Table 1**): — Glucose withdrawal leads to ROS accumulation and *p53*-mediated *Myc* repression. — Loss of *Myc* decreases *FoxM1,* a critical G2 transcription factor responsible for *Cdc25A/B*, as well as *Cyclin A* induction. — Positive feedback from *Cyclin A/Cdk2* aided by *Cdc25A/B* can keep an existing *FoxM1* pool active in G2 (**SM Fig. 6A**, *inset, gray arrows*), but glucose withdrawal interferes with this feedback and dooms the cell to an internal G1 reset. — Upon re-exposure to glucose, the cell starts another round of DNA replication (**SM Fig. 6A**, *bottom red circle*).	**SM Fig. 6A, 6B**	– *Indirect support:* ~ Harsh tumor environments involving both glucose withdrawal and acidosis resulted in a ~19.4% pool of survivor cells with 4N DNA content (7 days of nutrient withdrawal with acidosis) [92]. ~ 24 hours after nutrient restoration the fraction of G2/M cells briefly peak to a level that is consistent with pre-withdrawal levels (diploid cells reaching G2/M) *plus* the percentage of cells stuck with 4N DNA at day 7 of the withdrawal (potentially slower to re-enter the cell cycle) [92].
✳ Hyperfusion in response to glucose withdrawal, if it persists into mitosis, delays mitotic mitochondrial fragmentation long enough to cause spindle assembly defects and apoptosis.	**SM Fig. 6C**	– *Indirect support:* glucose-starved cells show a significant increase in spindle formation defects such as multipolar spindles [92].

3. Mitochondrial Dysfunction-Induced Senescence (MiDAS) is locked in by positive feedback, maintaining mitochondrial hyperfusion with low $\Delta\Psi_M$ and high ROS

To test whether our model can reproduce *irreversible* MiDAS, we first examined the steady states of the isolated Mitochondrial Module (automatic module isolation method in [50,53]). As **Figure 4A** indicates, this module acts as a three-state switch (has three distinct steady states). First, the ***healthy*** mitochondrial state (*top*) has no hyperfusion or excess fission. It has a healthy TCA cycle maintaining $\Delta\Psi_M$, ATP, and mitochondrial NAD$^+$ within their nominal range, keeping *AMPK* off, and mitophagy in its basal range (*Mitophagy_High* node is OFF). Second, mitochondria can get stuck in a ***fragmented*** state with low $\Delta\Psi_M$ and high mitochondrial ROS, leading to low ATP and active *AMPK*. As *AMPK* can phosphorylate and activate *Drp1* [93], this state is stabilized by a combination of *Drp1*-induced fission and a dynamic balance between high mitophagy and *PGC-1α*-induced mitochondrial biogenesis [62]. While *PGC-1α* induces *MFN1/2*, their ability to counterbalance fission and restore a healthy state is blocked by the molecular machinery of mitophagy [94,95].

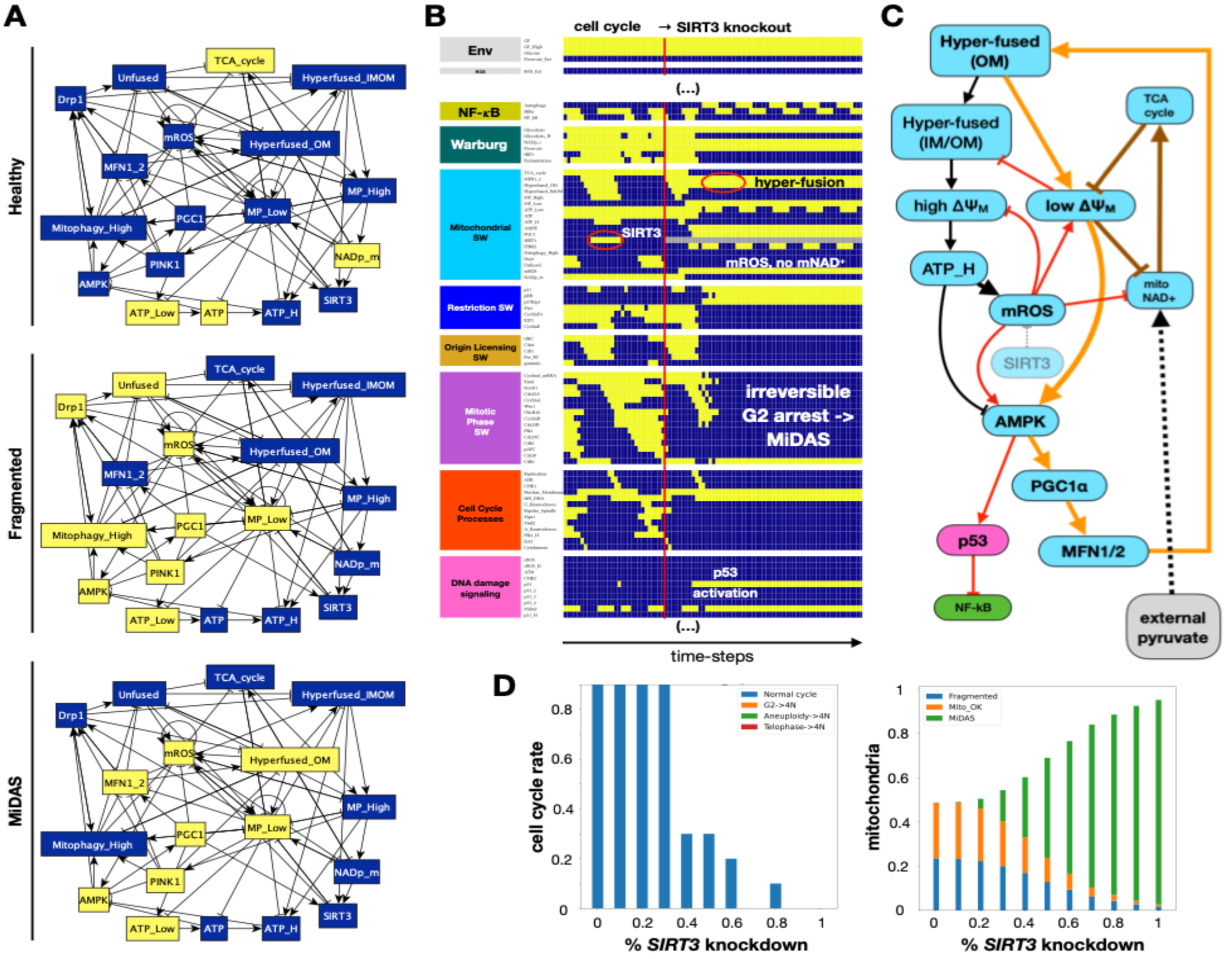

Figure 4. Model reproduces MiDAS in response to SIRT3 knockdown. A) Three stable states of the isolated mitochondrial module. *Yellow/dark blue background:* ON/OFF state of nodes in each stable state. **B)** Dynamics of relevant regulatory molecule expression/activity in a dividing cell responding to full *SIRT3*

knockout in early G1 (full network dynamics in **SM Fig. 7A**). *X-axis:* time-steps; *y-axis:* nodes organized by regulatory modules; *yellow/dark blue:* ON/OFF; *vertical red line:* start of *SIRT3* knockout; *red ovals*: SIRT3 expression during cell cycle (*left*) / hyperfused mitochondrial network in MiDAS (*right*); *labels:* relevant molecular or phenotypic changes in response to *SIRT3* knockout. **C)** Circuit responsible for locking in MiDAS following S-phase in *SIRT3*-null cells. *Light blue/pink/green nodes*: molecules from the mitochondrial/DNA damage/growth signaling modules. *Black links:* triggering event of MiDAS is a healthy but hyperfused network of mitochondria, responsible for high ATP generation during S phase but also mitochondrial-derived ROS (normally mitigated by *SIRT3*). *Red links:* in the absence of *SIRT3*, excess mitochondrial ROS damages the ETC, lowers $\Delta\Psi_M$ and consequently the mitochondrial $NAD^+/NADH$ ratio, and helps activate *AMPK.* At this point, two positive feedback loops engage to keep the mitochondrial network dysfunctional. *Orange links:* first positive feedback loop involving *AMPK*-mediated hyperfusion of the outer membrane ($AMPK \rightarrow PGC1\alpha \rightarrow MFN1/2$), no longer paired with inner membrane fusion and efficient ATP generation but still blocking its own disassembly (mitophagy) and subsequent renewal, which in turn keeps ATP low and *AMPK* active. *Brown links:* second positive feedback loop involving mitochondrial ROS-mediated damage to ETC proteins and mDNA, which keeps mitochondrial NAD^+ low, compromises the TCA cycle, and further lowers $\Delta\Psi_M$. *Black dashed link:* excess pyruvate can interrupt these feedback loops by restoring NAD^+ levels. **D)** Response of cells dividing in 95% saturating growth stimuli to increasing levels of *SIRT3* knockdown. *Top:* rate of normal cell cycle completion (*blue*) vs. G2 → G1 reset (*orange*, not observed), aberrant mitosis (*green*, not observed), or failed cytokinesis followed by genome duplication (*red*, not observed), relative to wild-type cell cycle (25 steps), shown as stacked bar charts. *Bottom:* fraction of time cells display normal mitochondria (*orange*), MiDAS (*green*), or fragmented mitochondria (*blue*). *Total sampled live cell time:* 50,000 steps; synchronous update; *Initial state for sampling runs:* cycling cell in high glucose and no external pyruvate, ROS, or *Trail.*

Third is a stable state that matches the experimentally observed signatures of ***MiDAS*** (*bottom*) [15]; it is characterized by low $\Delta\Psi_M$, low ATP and active *AMPK*, which in turn keeps *PGC-1α* active. Downstream of *PGC-1α*, increased *MFN1/2* keeps the outer mitochondrial membranes fused in a misplaced attempt to boost ATP levels via a hyperfused network (as seen in G1/S). Here, however, low $\Delta\Psi_M$ keeps *Opa1* from fusing the inner membranes [29], rendering the hyperfused network dysfunctional. This positive feedback from low $\Delta\Psi_M$ to *AMPK* to dysfunctional hyperfusion (and thus low $\Delta\Psi_M$) is stabilized by the fact that hyperfused mitochondria are refractory to mitophagy [45], compromising their usual renewal. Unlike the hyperfused state depicted in **Fig. 3B**, the model's MiDAS state is irreversible. A key difference between these two scenarios is the absence of *SIRT3* activity to mitigate mitochondrial ROS. While *PGC1α* can induce *SIRT3* [16], its activity depends on NAD^+, which requires a functioning ETC. Our model assumes that the combination of low $\Delta\Psi_M$ and mitochondrial ROS – which damages ETC components and mDNA – hinder the regeneration of the mitochondrial NAD^+ pool [96,97].

When incorporated into the rest of the network, the *Mitochondrial Module* must work in concert with the other modules in a way that preserves its phenotypic states and reproduces the experimentally observed commitment to MiDAS. To test this, we first knocked down *SIRT3* in a model cell undergoing rapid proliferation, a scenario shown to induce MiDAS [15]. Indeed, **Figure 4B** shows a permanent cell cycle arrest following *SIRT3* knockout, along with low mitochondrial $NAD^+/NADH$ ratio, active *AMPK* and *p53*, and no *NF-κB* activity – the reported hallmarks of MiDAS [15] (full time-course in **SM Fig. 7A**). In addition to reproducing these observed features, our model offers a mechanistic explanation for the transition (**Fig. 4C**), and several testable predictions related to *SIRT3* knockdown-induced MiDAS. Namely, we *predict* that *SIRT3*-null MiDAS cells have a hyperfused, non-functional mitochondrial network with low $\Delta\Psi_M$ and excessive ROS production; a phenotype also observed in damage-induced senescence [18].

Furthermore, we *predict* that these cells arrest in MiDAS from early G2 with 4N DNA content, and that G0 cells with access to glucose are protected from *SIRT3* knockout-induced MiDAS (**SM Fig. 7B**). In contrast, cells held in G0 by the lack of glucose with reversibly hyperfused mitochondria do enter MiDAS in response to *SIRT3* knockdown, as their ROS production increases and NAD^+ levels plummet (**SM Fig. 7C**).

In addition to *SIRT3* knockdown, the electron transport chain inhibitor rotenone and mtDNA depletion were also shown to trigger MiDAS, a response that culturing cells in excess pyruvate could prevent [15]. To test whether our model can reproduce these experiments, we first mimicked lowered ETC activity by forcibly lowering the model cell's $\Delta\Psi_M$. Indeed, loss of $\Delta\Psi_M$ at the G1/S boundary in a cell committed to cell cycle triggered MiDAS, an effect rescued by pyruvate (**SM Fig. 8,** *middle vs. right window*). External pyruvate also prevented MiDAS following the loss of *SIRT3* (**SM Fig. 9A**). Moreover, the model predicted that pyruvate could rescue wild-type cells from MiDAS (early senescence only), freeing them to enter the cell cycle when exposed to mitogens (**SM Fig. 9B**) or restoring ATP generation and their potential for future proliferation in quiescence (**SM Fig. 9C**). Further underscoring the key role of low $\Delta\Psi_M$ combined with mitochondrial hyperfusion, we have found that several perturbations described above for their role in disrupting the cell cycle can also trigger MiDAS – depending on their timing along the cycle. These include *Plk1* knockdown just before the cell clears the Spindle Assembly Checkpoint (SAC) (**SM Fig. 10A**), sub-lethal *Trail* exposure in cells pre-committed to the next cell cycle (**SM Fig. 10B**; late mitosis, starting hyperfusion for G1/S), and sub-lethal *Drp1* knockdown or mitochondrial hyperfusion in metaphase (**SM Fig. 10C-D**). The common predicted cause of MiDAS is a sub-lethal mitochondrial membrane permeabilization that lowers the $\Delta\Psi_M$ without activating executioner caspases (which would trigger apoptosis) – at a time when the mitochondria are hyperfused. As the cells they react to low $\Delta\Psi_M$ with *AMPK* activation, they lock in MiDAS.

4. External ROS exposure causes MiDAS, preventable by excess pyruvate

Given the central role of ROS in locking in MiDAS in *SIRT3*-null or ETC-deficient cells (**Fig. 4**), we next modeled the effects of extracellular ROS by linking an *ROS_Ext* environmental input to high intracellular ROS, as well as an immediate block on high $\Delta\Psi_M$. High internal ROS, in turn, activates *ATM/ATR, AMPK*, *p53* and autophagy, but also promotes mitochondrial dysfunction by interfering with the TCA cycle, lowering $\Delta\Psi_M$, and increasing mitochondrial ROS (**SM Fig. 11**). Exposing our dividing cells to prolonged pulses of external ROS reliably triggered MiDAS. Cells exposed to ROS in G1 arrested with 2N DNA content (**Figs. 5A, SM 12A**), while G2 cells lost their G2/M associated cyclin expression following sustained *p53* accumulation and underwent irreversible G2 arrest into MiDAS (**Figs. 5B, SM 12B**). Brief ROS exposure, in contrast, led to *reversible* G2 arrest followed by mitosis (**SM Fig. 13**); a difference our model captured via its four-node tracking of *p53* accumulation. Finally, our model predicted that quiescent cells were not as susceptible to ROS-induced MiDAS, owing their protection to continuous mitophagy (**Figs. 5C, SM 12C**). This was due to the lack of mitogen-induced AKT_H oscillations, aiding *FoxO1/3*-mediated mitophagy in blocking *MFN1/2*-driven hyperfusion. That said, cells that exited the cell cycle into MiDAS maintained MiDAS even in the absence of mitogens (**Figs. 5A-B,** *right*).

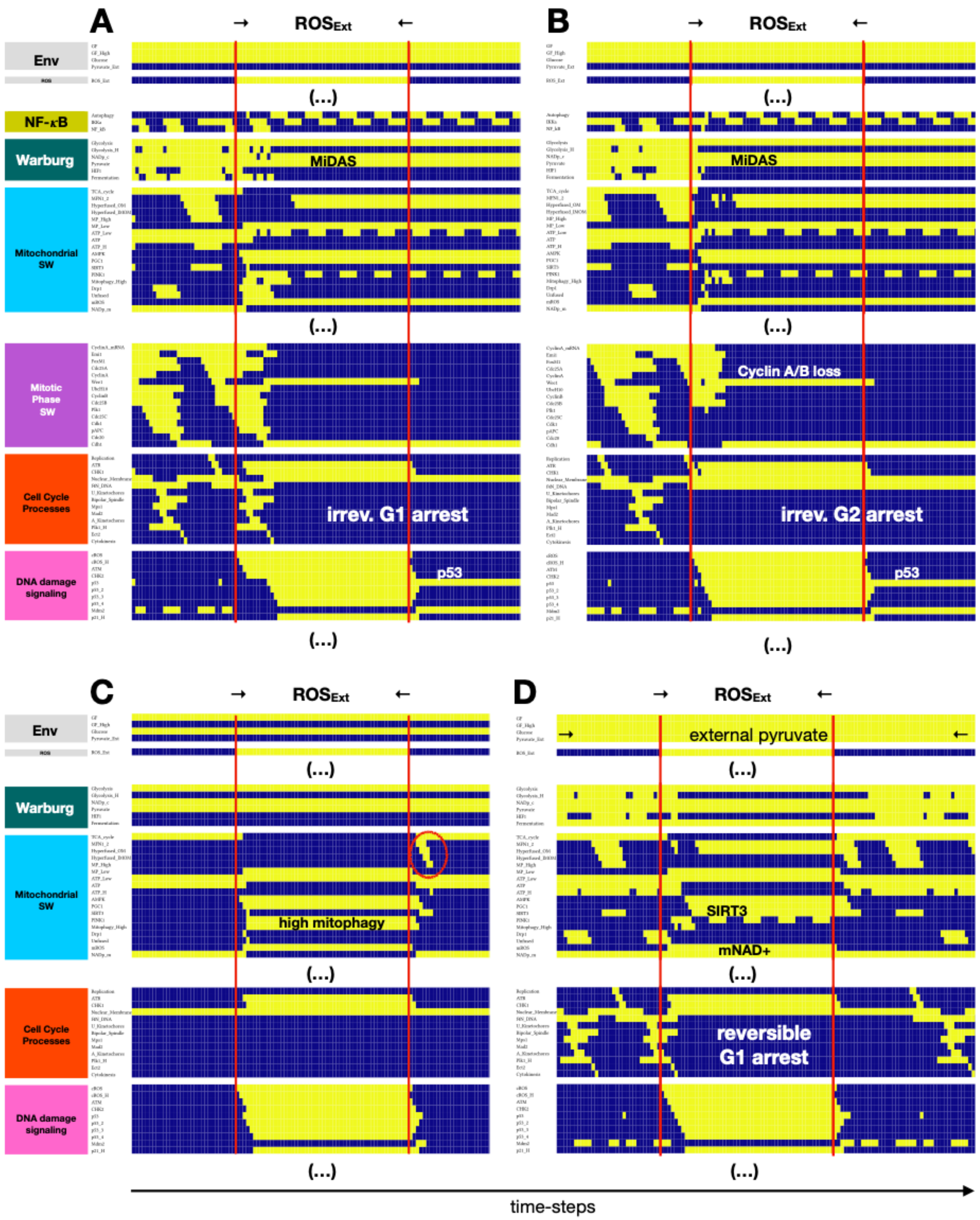

Figure 5. Model reproduces ROS-induced MiDAS in cycling cells and predicts protection from MiDAS in external pyruvate. A-B) Dynamics of relevant regulatory molecule expression/activity during exposure of a cycling cell to external ROS in (A) prometaphase, leading to cytokinesis followed by MiDAS (2N DNA), vs. (B) early G2, leading to irreversible G2 arrest and MiDAS with 4N DNA. **C)** Dynamics of relevant regulatory molecule expression/activity during exposure of a quiescent cell to external ROS, leading to high mitophagy and short-term hyperfusion to restore ATP levels. **D)** Dynamics of relevant regulatory molecule expression/activity during exposure of a cycling cell exposed to saturating levels of external pyruvate to

external ROS near the SAC, leading to reversible G1 arrest (cell cycle entry after external ROS is removed). *X-axis:* time-steps; *y-axis:* nodes organized by regulatory modules; *yellow/dark blue:* ON/OFF; *vertical red lines:* start/end of ROS exposure; *red oval on (C):* brief, homeostatic hyperfusion involving both outer and inner mitochondrial membranes; *white/black labels:* relevant molecular changes or outcomes; *full network dynamics:* **SM Fig. 12**.

Given that external pyruvate could protect *SIRT3*-knockout cells from MiDAS by maintaining NAD^+ levels, we next asked whether pyruvate could also prevent or reverse ROS-induced MiDAS. Indeed, excess pyruvate prevented the drop in mitochondrial NAD^+ observed in our ROS-exposed model cells, allowing NAD^+ dependent *SIRT3* activity to prevent MiDAS (**Fig. 5D**). To test whether *SIRT3* hyper-activation itself could act in a similar way, we simultaneously exposed our model cell to external ROS and forced *SIRT3* activation (**SM Fig. 14A**). Our model predicted that cells with hyperactive *SIRT3* were protected from ROS-induced MiDAS, and that forced *SIRT3* activation could reverse MiDAS (**SM Fig. 14B**). A similar result could be achieved by boosting NAD^+ levels (**SM Fig. 14C**) – previously shown to reverse MiDAS [15] and support pro-inflammatory SASP by restoring mitochondrial function in deep senescence [19,20].

5. The stability of MiDAS depends on the combinatorial influence of mitogens, glucose, ROS, and pyruvate

To examine the stability of MiDAS to perturbation in the cell's microenvironment, we examined our model's phenotypes (attractors) in every combination of its inputs and organized all relevant attractors representing live cells on a 4-dimensional input-space (**Fig. 6A**; sampling algorithm in [50]; full list of attractors in all environments in **SM File 6**; figure with every attractor in **SM Fig. 15**). For example, a quiescent cell exposed to basal growth signals, glucose, and no external ROS or pyruvate (*left panel, top, middle of front row, green-outlined cell*) is marked by a barcode showing the state of its key molecular switches: basal *PI3K* activity, normal mitochondria, a cell cycle machinery consistent with quiescence (restriction point not passed, G2/M cyclins off with a G0/G1 profile), apoptotic machinery off (survival state). The *green-outlined cell* to the right is a summary of this information: this state marks a healthy quiescent cell with dynamic mitochondria. In contrast, the cell cycle attractor (*left panel, top front row, red-outlined cell*) has a wide barcode showing oscillatory PI3K (*green*), dynamic mitochondria (*light blue*), a cyclic toggle of the Phase Switch (G1→G2→M, *purple*) and cell cycle events (*orange*) – we summarized this with a mitotic spindle icon (*red-outlined cell*).

As the left panel of **Fig. 6A** indicates, in conditions with sufficient glucose and no external ROS or pyruvate (*left panel, top front row*), our model predicts growth signal-dependent quiescence vs. cell cycle (*green- vs. red-bordered cells*). In addition, MiDAS cells are also stable in these environments, as expected from a non-reversible cell state (*static, hyperfused mitochondria, light, blue-bordered cells*). Loss of glucose, in contrast, sends healthy quiescent cells into a state characterized by energy stress with active *AMPK*, low $\Delta\Psi_M$, high mitophagy, and no hyperfusion (*left panel, bottom front row, green arrow* to *yellow-bordered cell*). Cycling cells, on the other hand, generally arrest in a state with reversible mitochondrial hyperfusion, distinguished from MiDAS by *SIRT3* mediated control of ROS paired with NAD^+ maintenance (*red arrow* to *orange-bordered cell;* see **Fig. 3A**), Indeed, this state is reversible by glucose exposure — either during cell cycle re-entry (*bidirectional red arrow*), or quiescence (*orange arrow* to low growth factors, followed by *green* to normal glucose).

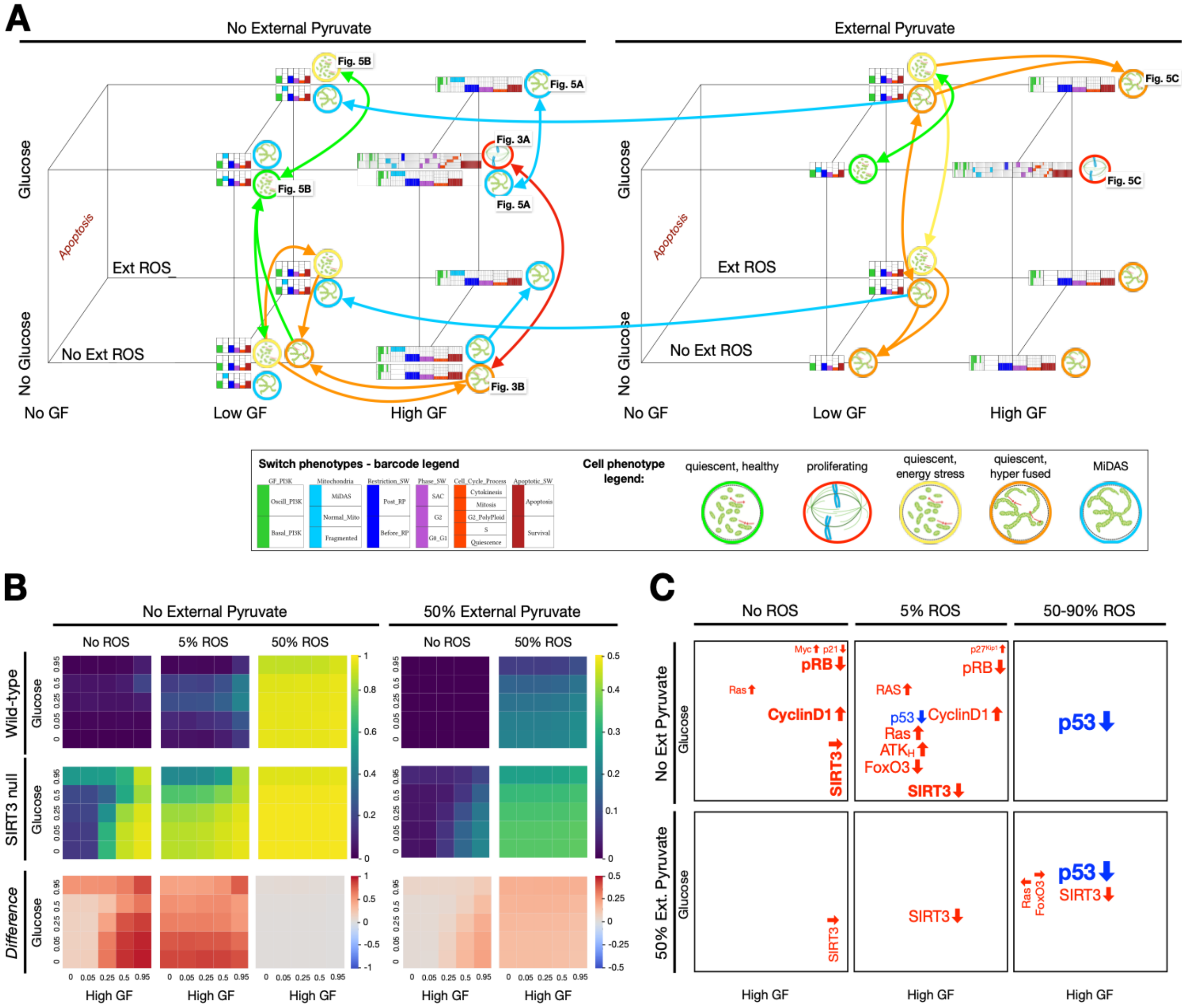

Figure 6. Model produces a heterogeneous mix of cell phenotypes modulated by mitogen, glucose, ROS, and pyruvate exposure, and shifts in the presence of cancer-related mutations. A) Summary of model cell states detected in every combination of no/low/high growth-factor (*x axis*), absence/presence of external ROS (*y axis*), low/high glucose (*z axis*), and absence/presence of external pyruvate (*left/right*). Apoptotic and tetraploid quiescent cell states were omitted for clarity (all attractors: **SM Fig. 15**, **SM File 6**). Barcodes representing each attractor were derived by comparing the expression of nodes in relevant modules to predetermined molecular signatures (e.g., apoptosis vs. survival) and encoded in the model's *.dmms* file (barcode legend, *bottom left*). Oscillatory phenotypes have expanded barcodes that mark the transitions their regulatory switches undergo during the cycle (*left, high GF area*). Visual summaries of overall cell states indicate the shape and dynamics of the mitochondrial network, distinguish quiescent vs. cycling cells, as well as normal vs. dysfunctional mitochondria (cell phenotype legend, *bottom right*). *Figure labels:* time-courses with molecule-level view of state. *State transition arrows: light blue:* irreversible transition to MiDAS; *green:* reversible transitions from quiescence with healthy mitochondria & transition to it; *orange:* transitions between energy stressed non-MiDAS states; *red:* reversible cell cycle arrest upon glucose withdrawal. **B)** Fraction of time cells spend in a MiDAS state at varying levels of mitogen stimulation (*x* axis) and glucose (*y* axis) with no (0%), mild (5%) or strong (50%) ROS exposure, in the absence (left 3 columns) vs. presence of 50% external pyruvate (right 2

column). *Top/middle row:* wild-type/*SIRT3* null cells; *bottom row:* increase in the fraction of time spent in MiDAS in *SIRT3*-null cells. *Length of time-window for continuous runs:* 100 steps (10 wild-type cell cycle lengths); *total sampled live cell time:* 500,000 steps; synchronous update; *initial state for sampling runs:* cycling cell in high glucose and no external pyruvate, ROS, or *Trail*. **C)** Summary of changes to the frequency of MiDAS across 4 environmental dimensions for 13 oncogenic and 11 tumor-suppressive mutations [98] (data in **SM File 13**). *Top vs. bottom rows:* no external pyruvate vs. 50% of saturating external pyruvate for no ROS vs. mild (5%) vs. strong (50% to 95%) external ROS. *Gene label position:* area of growth factor/glucose environment map where the mutation's effects are strongest; *red/blue:* mutation increases/decreases the frequency of MiDAS; *up/down arrows after gene:* knockdown/hyper-activation; *font size:* approximate effect strength. *Image credits:* apoptotic cell: *https://en.wikiversity.org/wiki/WikiJournal_of_Medicine/Cell_disassembly_during_apoptosis*; mitochondrial networks: PMID 25847815; mitotic spindle: *https://en.wikipedia.org/wiki/Spindle_apparatus*.

Unlike glucose withdrawal, ROS exposure in the presence of strong growth signals always results in MiDAS (*light-blue arrows*). Low growth signals protect quiescent cells from ROS-induced MIDAS; instead, these enter an energy-stressed state (*yellow-bordered cells*). Access to glucose keeps this stressed state reversible upon relief from ROS (*green arrow, top plane, middle*). In the absence of glucose, however, cells recovering from ROS get stuck with a hyperfused state that is not quite MiDAS (*orange arrows, bottom plane, middle*), given that subsequent glucose exposure can reestablish healthy mitochondria (*green up-arrow, front plane*). Meanwhile, the MiDAS phenotype remains stable across all environments without pyruvate. The presence of pyruvate drastically changes the fate of our model cells (**Fig. 6A**, *right panel*). While cell cycle entry and exit remain unaltered (*green- & red-outlined cells*), in low glucose / no ROS even quiescent cells can't avoid reversible hyperfusion (*orange-outlined cells, bottom front row*). That said, MiDAS disappears completely in favor of this reversible fate, and the loss of pyruvate only triggers MiDAS from this hyperfused state in the presence of ROS (*light-blue arrows*).

6. Oncogene hyperactivation and tumor suppressor loss (except p53) tend to increase MiDAS in the absence of external pyruvate

To probe the effect of mutations such as *SIRT3* loss on the full phenotype-repertoire of our model, we measured the average time spent in a MiDAS state during a 250-step (10 cell cycle length) window upon entering a new environment, which varied along a four-dimensional grid of external conditions. First, we measured the prevalence of MiDAS for every combination of *GF_High*, *Glucose*, and *ROS_Ext* at 0, 5%, 25%, 50%, and 95% saturation with no external pyruvate, then we repeated the full scan for 50% and 100% pyruvate. **Figure 6B** shows the relevant heat maps, comparing wild-type cells (*top row*) to those in which we knock out *SIRT3* at time 0 (*middle row*). The change caused by *SIRT3* knockdown (*bottom row*) indicates that in the absence of external ROS (*leftmost column*) *SIRT3* knockdown boosts MiDAS most in high growth factor / low glucose environments, though its effects are strong in all mitogen-stimulated cells. In contrast, very mild ROS (5%, *middle*) renders the effects of *SIRT3* knockdown nonlinear, as it now affects low-growth factor/low glucose cells as much as high-growth factor/high glucose exposed ones. Strong ROS, in contrast, erases the effects of *SIRT3* (it drives MiDAS regardless). 50% pyruvate tempers the *SIRT3* effect (*rightmost columns;* see ***SM File 13*** for full dataset), while 100% completely blocks MiDAS (**Fig. 6A**).

Next we repeated this experiment on 13 oncogenic and 11 tumor-suppressive mutations from the top 500 of cancer-driver genes across human cancers for which our model has a corresponding node (**SM File 13;** hyper-activated: *PI3K*$_H$*, Ras, RAF, mTORC1, AKT*$_H$*, Myc, HIF1, MEK, Cyclin E, Cyclin D1, ERK, p21*$_H$*, p27*^{Kip1}; knocked out: *p53, ATM, ATR, RB, p21, TSC2, FoxO1, FoxO3, Caspase 8, Caspase 9*) [98]. We summarized our findings using an abstract version of the 4D environmental space, placing the name of protooncogenes and/or tumor suppressors that *altered* the model's tendency to enter MiDAS into the position in environment-space where their effect was strongest (**Fig. 6C**). Thus, *SIRT3* knockdown appears in red (it up-regulates MiDAS), and its effect is most pronounced in high GF, low glucose, and no pyruvate (*bold SIRT3 labels*). In contrast, *p53* knockdown reduces ROS-induced MiDAS in all conditions (*blue p53 labels*, **SM Fig. 16**), in line with experimental data showing that p53 is required for mitochondrial hyperfusion in senescent cells [18]. Overall, our model predicts that oncogene activation or tumor suppressor loss that helps bypass the G1/S checkpoint (excess *Cyclin D1, Ras, AKT*$_H$*, Myc;* loss of *pRB, FoxO3* or *p21*) increases the incidence of MiDAS, especially in mild ROS not capable of triggering MiDAS in quiescent cells. The remaining mutations have no effect on the time our model cells spent in MiDAS in any condition, though many altered cell cycle progression and/or apoptosis as expected (loss of *FoxO1, Casp8, Casp9, TSC2;* activation of *ERK, PI3K*$_H$ or *p21*$_H$; instructions to run simulations in **SM File 11**). The only cancer-associated mutation that reduced MiDAS in our model was *p53* knockdown (**Fig. 6C, SM File 13**).

Discussion

Our model brings together insights from the in-depth MiDAS study in [15] and a wide variety of experimental data on mitochondrial dynamics during cell cycle, apoptosis, and DNA damage-induced senescence with a previously published Boolean network model of cell cycle control linked to apoptosis [47]. The resulting 134-node Boolean model (**Fig. 2**) is novel in that it **a)** reproduces the two-way connection between cell cycle progression and mitochondrial dynamics (**Fig. 3A**), **b)** accounts for the role of mitochondrial fragmentation in apoptosis (including mitotic catastrophe, **SM Fig. 2**), **c)** reproduces the reversible hyperfusion observed in glucose-starved cells (**Fig. 3B**), **d)** matches experimental data on *SIRT3* knockout and mitochondrial damage-induced MiDAS, including the role of NAD$^+$ and its rescue by external pyruvate (**Fig. 4**), and **e)** models ROS-induced MiDAS as a part of the first stage of a DNA-damage mediated senescence program (**Fig 5**).

Our model offers a series of testable predictions:

a) In cell lines with low basal *p21* expression known to pre-commit to the next division in early mitosis (e.g., MCF10A cells) [72], a subset of cells respond to glucose withdrawal by arresting with 4N DNA content but losing their internal G2 state (i.e. *Cyclin A/B* expression), then undergo endo-reduplication upon glucose re-exposure. A study by Dai et. al. focusing on chromosomal instability in harsh tumor environments, involving glucose withdrawal as well as acidosis, provides indirect support for the feasibility of this prediction [92]. The authors observed that ~19.4% of the cells surviving 7 days of nutrient withdrawal (with acidosis) were arrested with 4N DNA content (Fig. 8A/B in [92]). Moreover, 24 hours after nutrient restoration the fraction of G2/M cells briefly peaked to a level that is consistent with pre-withdrawal levels (diploid cells now in G2/M) plus the percentage of cells stuck with 4N DNA at day 7 of the withdrawal (potentially slower to re-enter the cell cycle). Based on this we predict that a small fraction of rapidly dividing cells become tetraploid in response to glucose withdrawal via the molecular mechanism described in **Table 1C** (**SM Fig. 6A**). This could be tested by monitoring the ploidy of MCF10A cells exposed to strong mitogens, along with cyclic glucose withdrawal / re-exposure. Testing our predicted molecular mechanism would require monitoring *FoxM1* mRNA, *FoxM1* protein and its *Cdk*-mediated phosphorylation, and showing that a subpopulation with lower *FoxM1* expression/activity at the end of S phase arrest with 4N DNA, then re-enter S-phase upon glucose exposure.

b) In a subset of glucose-starved cells that pass the G2/M checkpoint with hyperfused mitochondria, mitotic fragmentation can be delayed sufficiently to cause spindle assembly defects and mitotic catastrophe (**SM Fig. 6B-C**). While this prediction depends on the relative speed of mitochondrial dynamics versus lethal spindle assembly defects (and thus could be a modeling artifact), a significant increase in spindle formation defects such as multipolar spindles were documented in glucose-starved cells [92]. A follow-up live imaging experiment could test our proposed mechanism (i.e., lack of timely mitochondrial fission) as well as their eventual outcome (*Caspase 2*-mediated apoptosis).

c) In our model, the molecular drivers of MiDAS, such as the loss of *SIRT3*, rely on the feedback between hyperfusion, low mitophagy and mitochondrial damage caused by high ROS/low NAD^+. This proposed mechanism leads to several related predictions: ***i)*** mitochondria in *SIRT3*-null cells that enter *MiDAS* are hyperfused, with low $\Delta\Psi_M$ / high mROS (**Fig. 4**); ***ii)*** *SIRT3*-null cells arrest in *MiDAS* from G2, with 4N DNA content (**Fig. 4B**); ***iii)*** quiescent cells with access to glucose are less susceptible to *SIRT3* loss- and ROS-induced MiDAS due to *FoxO*-mediated mitophagy, which blocks *MFN1/2* from inducing hyperfusion (**SM Fig. 7B**). ***iv)*** glucose-starved quiescent cells enter MiDAS in response to *SIRT3* knockdown (**SM Fig. 7C**). These predictions can be tested by monitoring mitochondrial morphology, $\Delta\Psi_M$, and *MFN1/2* localization in response to *SIRT3* loss, as well as H_2O_2 exposure in conditions involving various combinations of growth stimuli and glucose.

d) MiDAS cells that have not yet established deep senescence (i.e. 2-3 days post induction by *SIRT3* knockdown or ROS) are rescued from MiDAS by subsequent pyruvate exposure (**SM Figs. 8-9**), or by forced *SIRT3* activation (**SM. Fig. 14B**). This parallels the MiDAS rescue by NAD^+ precursor nicotinamide mononucleotide [15], or the increased expression of *NAMPT* in deep senescence required for proper SASP production [19]; both of which restore NAD^+ (**SM. Fig. 14C**).

e) Cycling cells with hyperfused mitochondria near the G1/S boundary are highly susceptible to sub-lethal apoptotic signals that briefly lower $\Delta\Psi_M$ but do not cause significant effector caspase activation (**SM Fig. 10**). A study documenting minority MOMP in senescent cells offers some indirect support to this prediction [89]. Minority MOMP only occurs in a small subset of mitochondria, it involves loss of $\Delta\Psi_M$ and some cytochrome C leakage but no commitment to apoptosis, similar to the model's dynamics. That said, a causal relationship between minority MOMP and senescence entry and/or MiDAS has not been established.

f) Our cancer-related mutations screen predicts that the activation of oncogenes and/or loss of tumor suppressors that result in G1/S bypass tend to increase MiDAS, an effect blocked by saturating pyruvate exposure (**Fig. 6C**). These include *Cyclin D1, Ras,* AKT_H , or *Myc* hyperactivation, and *pRB, FoxO3* or *p21* loss. A notable exception, as expected from the literature, is *p53* loss, which blocks MiDAS [18].

To achieve a model complexity capable of reproducing the above range of observed cell behaviors, we found the Boolean modeling approach necessary as a constraint on the network's dynamical rules. The type of data that could effectively constrain a large number of parameters needed for a concentration-based (continuous) model, such as detailed kinetic data on individual interactions and/or fine-grained time courses of molecular changes, are not currently available. That said, the Boolean framework is not without limitations. Key among these is the challenge of capturing dynamic homeostatic equilibria, such as the precise balance of mitochondrial fission and fusion that keeps cells healthy. While we account for *cell-wide* shifts in the balance leading to hyperfusion or excess fragmentation, our model does not capture subtler changes to mitochondrial dynamics such as the rapid, flexible fusion/fission cycle seen in dividing cells versus the more frozen morphology in aging cells [25]. Related to this, we purposefully left out *PGC1α* activation by *mTORC1* [99], as this would force our model to activate *MFN1/2* any time *mTORC1* was active, and either cause hyperfusion well ahead of the G1/S boundary or require us to also account for *mTORC1*'s effect on increasing *Drp1*-driven fission. Overall, it appears that *mTORC1* balances the induction of mitochondrial biogenesis downstream of *PGC1α* with increased fission [100], rendering the mitochondrial network more dynamic but not hyperfused. Here we chose to omit this balancing act, and thus are likely missing the role of *mTORC1* in the induction and maintenance of senescence.

Another limitation / boundary of our model's applicability, albeit by design, is that it does not address the processes leading to deep senescence. This design allowed us to examine the conditions and feedback loops that drive mitochondrial dysfunction and stabilize MiDAS in a modular way, without the parallel influence of *p53*- and *p21*-dependent changes leading to damage-induced deep-senescence [13]; clearly distinct from MiDAS [15]. Briefly, the omitted process involves high *p21*-mediated *p38* MAPK activation, leading to increased cytosolic ROS that locks in a *p21* → *p38* → ROS & *p21* feedback loop [13]. This in turn damages DNA (and mitochondria). The loop is stable without ongoing *p53* activity, maintains early senescence [101], and slowly activates deep-senescence promoting transcription via *FoxA1*, *HBP1*, and *HMGA1*, up-regulating *p16* [22,102,103]. Together they assemble Senescence-Associated Heterochromatin Foci (SAHF), creating deep senescence. At this point, about 7 days following the initial damage *HMGA1* induces *NAMPT* [19], while an unknown process downregulates *p53* [24]. The resulting functional mitochondria and *NF-κB* reactivation change the SASP from primarily growth- and EMT-promoting (growth factors, *TGFβ*) to pro-inflammatory (*IL-1/6/8*) [104].Without these pathways the phenotypic predictions of our model related to the fate of wild-type or mutant cells are limited to predicting MiDAS. The drawback is that the reversal of MiDAS in our model can reestablish proliferative capacity (**SM Fig. 14**), while cells *in vitro* remain arrested and senescent due to the non-mitochondrial *p21/p38/*ROS feedback [13]. Thus, incorporating this deep-senescence circuit downstream of ionizing radiation and/or UV DNA damage is an immediate future direction. The main challenges are the unknown mechanisms that lower *p53* in deep senescence, and delineating the precise conditions that control the boundary between non-lethal vs. lethal damage, as the latter is known to be cell-type specific [105].

Our model raises the intriguing question: is MiDAS always reversed in deep senescence? Our model implicitly assumes that if and when NAD$^+$ levels are restored, the cell's mitochondria have an adequate reservoir of healthy mtDNA to cycle out of their dysfunctional state via enhanced mitophagy and mitochondrial biogenesis. Yet, sustained oxidative stress compromises mtDNA, and while mitochondria can tolerate a high mutation load, the system has a breaking point that permanently crashes the $\Delta\Psi_M$ [106]. Thus, we expect a population of cells to respond to both the initial DNA damage and the subsequent chronically high ROS in a heterogeneous manner, generating some cells that reverse MiDAS to establish a canonical pro-inflammatory SASP alongside others that remain permanently stuck. Given the role of a pro-inflammatory SASP in recruiting the immune cells that clear senescent cells from a healthy tissue [7], we can further ask: *can deep-senescent MiDAS cells hide from the immune system?* This could provide a mechanism for the observed decline of senescent cell clearance with age [107]. Due to their enhanced ROS production, MiDAS cells may also be responsible for the population-dependent increase in senescent cell accumulation [108], shown to explain organism-level features of aging [109]. We expect mutations in a tumor setting to boost this heterogeneity, as several cancer-associated mutations guarantee permanent MiDAS (**Fig. 6C**). A stochastic version of our model with a weak noisy link from mitochondrial ROS to an mtDNA node that eventually shuts off the ETC and locks the system into a low-$\Delta\Psi_M$ state could model this heterogeneity. Such a model would support the Stochastic Step Model of Replicative Senescence [110], offering specific molecular mechanisms responsible for tissue homeostasis versus aging.

A long-term goal is to model cellular heterogeneity within a multicellular tissue. With our Boolean models at its heart, a multi-scale model of tissue homeostasis, aging, or cancer evolution could bring clarity to the structure of cellular heterogeneity, division of labor, and cooperation in micro-environments characteristic to each. Ideally done after deep senescence is accounted for, this project could bring together the conceptual clarity of population-only tissue aging models [109,110] with the predictive power displayed by earlier efforts at such multi-scale integration based on the models of mitochondrial dysfunction that inspired ours [25]. This multi-scale model could then examine the interplay between healing (involving damage, apoptosis, senescence, as well as cell cycle entry) and aging (involving senescent cell accumulation). Furthermore, it could help probe the effects of cancer microenvironments on the behavior and heterogeneity of genetically identical cells (e.g., glucose and pyruvate availability and its effects on susceptibility to ROS [111]). Tying it all together, this multi scale model could predict the direct and/or combinatorial contribution of several cancer-associated mutations on cancer evolution, along with their ability to alter healing and aging in a tumor's neighborhood.

Acknowledgements

The authors would like to thank Ruthie Ressler for providing a Notepad++ language module for *.dmms* and *.vex* files.

Funding: This work was supported by the College of Wooster, including the Henry Luce III Fund for Distinguished Scholarship (E.R.), Henry J. Copeland Independent Study Fund (H.S. and M.H.), Faculty Development funds, and student conference travel support. D.D and K.G. were supported by the National Institutes of Health [grant number HL155749].

Author Contributions

H.S. — Conceptualization, Data curation; Formal analysis; Investigation; Writing - review & editing (designed the first version of a Boolean MiDAS switch, recognizing the relationship between hyperfusion, reduced mitophagy and senescence; provided revisions and manuscript edits).

D.D. — Data curation; Formal analysis; Investigation; Writing - review & editing (helped refine the MiDAS module, build metabolic inputs accounting for the dynamics of NAD$^+$; edited/restructured manuscript).

M.H. — Data curation; Formal analysis; Investigation (worked on the integration of the MiDAS module with cell cycle control and apoptosis).

K.F. — Data curation; Formal analysis; Investigation; Writing - review & editing (worked on the integration of the MiDAS module with cell cycle control and apoptosis, edited manuscript).

P.L.R. — Software; Visualization; Writing - review & editing (developed the *dynmod* software package that simulated the model's dynamical behavior, edited manuscript).

K.G. — Supervision; Resources (supported and supervised D.D., edited manuscript).

E.R.R. — Project administration; Conceptualization, Data curation; Formal analysis; Investigation; Visualization; Software; Resources; Writing - original draft (helped conceive project, supervised H.S., M.H., K.F. and P.L.R., acquired funding, developed the *Boolean_code_for_MiDAS* software, analyzed/refined final model and drafted the paper).

References

[1] SEER Cancer Statistics Review, 1975-2018, National Cancer Institute. Bethesda, MD, 2011.

[2] R. Di Micco, V. Krizhanovsky, D. Baker, and F. d'Adda di Fagagna, *Cellular Senescence in Ageing: From Mechanisms to Therapeutic Opportunities*, Nat Rev Mol Cell Biol **22**, 75 (2021).

[3] D. McHugh and J. Gil, *Senescence and Aging: Causes, Consequences, and Therapeutic Avenues*, J Cell Biol **217**, 65 (2018).

[4] J. Campisi, *Aging, Cellular Senescence, and Cancer*, Annu Rev Physiol **75**, 685 (2013).

[5] J. Campisi, *Senescent Cells, Tumor Suppression, and Organismal Aging: Good Citizens, Bad Neighbors*, Cell **120**, 513 (2005).

[6] H. N. Wilkinson and M. J. Hardman, *Senescence in Wound Repair: Emerging Strategies to Target Chronic Healing Wounds*, Front Cell Dev Biol **8**, 773 (2020).

[7] L. G. P. L. Prata, I. G. Ovsyannikova, T. Tchkonia, and J. L. Kirkland, *Senescent Cell Clearance by the Immune System: Emerging Therapeutic Opportunities*, Semin Immunol **40**, 101275 (2018).

[8] G. Nelson, J. Wordsworth, C. Wang, D. Jurk, C. Lawless, C. Martin-Ruiz, and T. von Zglinicki, *A Senescent Cell Bystander Effect: Senescence-Induced Senescence*, Aging Cell **11**, 345 (2012).

[9] N. Sun, R. J. Youle, and T. Finkel, *The Mitochondrial Basis of Aging*, Mol Cell **61**, 654 (2016).

[10] S. Srivastava, *The Mitochondrial Basis of Aging and Age-Related Disorders*, Genes (Basel) **8**, 398 (2017).

[11] S. Miwa, S. Kashyap, E. Chini, and T. von Zglinicki, *Mitochondrial Dysfunction in Cell Senescence and Aging*, J Clin Invest **132**, e158447 (2022).

[12] S. Lee, S.-Y. Jeong, W.-C. Lim, S. Kim, Y.-Y. Park, X. Sun, R. J. Youle, and H. Cho, *Mitochondrial Fission and Fusion Mediators, hFis1 and OPA1, Modulate Cellular Senescence*, J Biol Chem **282**, 22977 (2007).

[13] J. F. Passos et al., *Feedback between P21 and Reactive Oxygen Production Is Necessary for Cell Senescence*, Mol Syst Biol **6**, 347 (2010).

[14] R. G. Jones, D. R. Plas, S. Kubek, M. Buzzai, J. Mu, Y. Xu, M. J. Birnbaum, and C. B. Thompson, *AMP-Activated Protein Kinase Induces a P53-Dependent Metabolic Checkpoint*, Mol Cell **18**, 283 (2005).

[15] C. D. Wiley et al., *Mitochondrial Dysfunction Induces Senescence with a Distinct Secretory Phenotype*, Cell Metabolism **23**, 303 (2016).

[16] X. Kong, R. Wang, Y. Xue, X. Liu, H. Zhang, Y. Chen, F. Fang, and Y. Chang, *Sirtuin 3, a New Target of PGC-1alpha, Plays an Important Role in the Suppression of ROS and Mitochondrial Biogenesis*, PLoS One **5**, e11707 (2010).

[17] H. C. D. Medeiros and S. Y. Lunt, *The Warburg Effect: Saturation of Mitochondrial NADH Shuttles Triggers Aerobic Lactate Fermentation*, Mol Cell **82**, 3119 (2022).

[18] Y. Y. Kim, J.-H. Um, J.-H. Yoon, D.-Y. Lee, Y. J. Lee, D. H. Kim, J.-I. Park, and J. Yun, *P53 Regulates Mitochondrial Dynamics by Inhibiting Drp1 Translocation into Mitochondria during Cellular Senescence*, FASEB J **34**, 2451 (2020).

[19] T. Nacarelli et al., *NAD+ Metabolism Governs the Proinflammatory Senescence-Associated Secretome*, Nat Cell Biol **21**, 397 (2019).

[20] C. Correia-Melo et al., *Mitochondria Are Required for Pro-Ageing Features of the Senescent Phenotype*, EMBO J **35**, 724 (2016).

[21] J.-P. Coppé, C. K. Patil, F. Rodier, Y. Sun, D. P. Muñoz, J. Goldstein, P. S. Nelson, P.-Y. Desprez, and J. Campisi, *Senescence-Associated Secretory Phenotypes Reveal Cell-Nonautonomous Functions of Oncogenic RAS and the P53 Tumor Suppressor*, PLoS Biol **6**, 2853 (2008).

[22] M. Narita, M. Narita, V. Krizhanovsky, S. Nuñez, A. Chicas, S. A. Hearn, M. P. Myers, and S. W. Lowe, *A Novel Role for High-Mobility Group a Proteins in Cellular Senescence and Heterochromatin Formation*, Cell **126**, 503 (2006).

[23] J. R. Revollo, A. A. Grimm, and S. Imai, *The Regulation of Nicotinamide Adenine Dinucleotide Biosynthesis by Nampt/PBEF/Visfatin in Mammals*, Curr Opin Gastroenterol **23**, 164 (2007).

[24] J.-H. Chen and S. E. Ozanne, *Deep Senescent Human Fibroblasts Show Diminished DNA Damage Foci but Retain Checkpoint Capacity to Oxidative Stress*, FEBS Lett **580**, 6669 (2006).

[25] P. Dalle Pezze, G. Nelson, E. G. Otten, V. I. Korolchuk, T. B. L. Kirkwood, T. von Zglinicki, and D. P. Shanley, *Dynamic Modelling of Pathways to Cellular Senescence Reveals Strategies for Targeted Interventions.*, PLoS Computational Biology **10**, e1003728 (2014).

[26] V. Parra, H. Verdejo, A. del Campo, C. Pennanen, J. Kuzmicic, M. Iglewski, J. A. Hill, B. A. Rothermel, and S. Lavandero, *The Complex Interplay between Mitochondrial Dynamics and Cardiac Metabolism*, J Bioenerg Biomembr **43**, 47 (2011).

[27] C.-H. Yao, R. Wang, Y. Wang, C.-P. Kung, J. D. Weber, and G. J. Patti, *Mitochondrial Fusion Supports Increased Oxidative Phosphorylation during Cell Proliferation*, Elife **8**, e41351 (2019).

[28] K. Mitra, C. Wunder, B. Roysam, G. Lin, and J. Lippincott-Schwartz, *A Hyperfused Mitochondrial State Achieved at G1-S Regulates Cyclin E Buildup and Entry into S Phase*, Proc Natl Acad Sci U S A **106**, 11960 (2009).

[29] E. Q. Toyama et al., *Metabolism. AMP-Activated Protein Kinase Mediates Mitochondrial Fission in Response to Energy Stress*, Science **351**, 275 (2016).

[30] L. C. Gomes, G. Di Benedetto, and L. Scorrano, *During Autophagy Mitochondria Elongate, Are Spared from Degradation and Sustain Cell Viability*, Nat Cell Biol **13**, 589 (2011).

[31] D. Tondera et al., *SLP-2 Is Required for Stress-Induced Mitochondrial Hyperfusion*, EMBO J **28**, 1589 (2009).

[32] N. Taguchi, N. Ishihara, A. Jofuku, T. Oka, and K. Mihara, *Mitotic Phosphorylation of Dynamin-Related GTPase Drp1 Participates in Mitochondrial Fission*, J. Biol. Chem. **282**, 11521 (2007).

[33] R. Horbay and R. Bilyy, *Mitochondrial Dynamics during Cell Cycling*, Apoptosis **21**, 1327 (2016).

[34] E. J. Pereira, C. M. Smolko, and K. A. Janes, *Computational Models of Reactive Oxygen Species as Metabolic Byproducts and Signal-Transduction Modulators*, Front Pharmacol **7**, 457 (2016).

[35] V. A. Selivanov, T. V. Votyakova, J. A. Zeak, M. Trucco, J. Roca, and M. Cascante, *Bistability of Mitochondrial Respiration Underlies Paradoxical Reactive Oxygen Species Generation Induced by Anoxia*, PLoS Comput Biol **5**, e1000619 (2009).

[36] L. D. Gauthier, J. L. Greenstein, S. Cortassa, B. O'Rourke, and R. L. Winslow, *A Computational Model of Reactive Oxygen Species and Redox Balance in Cardiac Mitochondria*, Biophys J **105**, 1045 (2013).

[37] M. A. Aon, B. A. Stanley, V. Sivakumaran, J. M. Kembro, B. O'Rourke, N. Paolocci, and S. Cortassa, *Glutathione/Thioredoxin Systems Modulate Mitochondrial H2O2 Emission: An Experimental-Computational Study*, J Gen Physiol **139**, 479 (2012).

[38] J. N. Bazil, D. A. Beard, and K. C. Vinnakota, *Catalytic Coupling of Oxidative Phosphorylation, ATP Demand, and Reactive Oxygen Species Generation*, Biophys J **110**, 962 (2016).

[39] J. Park, J. Lee, and C. Choi, *Mitochondrial Network Determines Intracellular ROS Dynamics and Sensitivity to Oxidative Stress through Switching Inter-Mitochondrial Messengers*, PLoS One **6**, e23211 (2011).

[40] A. M. Guimera, P. Clark, J. Wordsworth, S. Anugula, L. J. Rasmussen, and D. P. Shanley, *Systems Modelling Predicts Chronic Inflammation and Genomic Instability Prevent Effective Mitochondrial Regulation during Biological Ageing*, Exp Gerontol **166**, 111889 (2022).

[41] Z. Y. Tam, J. Gruber, B. Halliwell, and R. Gunawan, *Mathematical Modeling of the Role of Mitochondrial Fusion and Fission in Mitochondrial DNA Maintenance*, PLoS One **8**, e76230 (2013).

[42] G. Dalmasso, P. A. Marin Zapata, N. R. Brady, and A. Hamacher-Brady, *Agent-Based Modeling of Mitochondria Links Sub-Cellular Dynamics to Cellular Homeostasis and Heterogeneity*, PLoS One **12**, e0168198 (2017).

[43] K. Kornick, B. Bogner, L. Sutter, and M. Das, *Population Dynamics of Mitochondria in Cells: A Minimal Mathematical Model*, Front. Phys. **7**, 146 (2019).

[44] T. E. Hoffman, K. J. Barnett, L. Wallis, and W. H. Hanneman, *A Multimethod Computational Simulation Approach for Investigating Mitochondrial Dynamics and Dysfunction in Degenerative Aging*, Aging Cell **16**, 1244 (2017).

[45] A. S. Rambold, B. Kostelecky, N. Elia, and J. Lippincott-Schwartz, *Tubular Network Formation Protects Mitochondria from Autophagosomal Degradation during Nutrient Starvation*, Proc Natl Acad Sci U S A **108**, 10190 (2011).

[46] S. S. Korshunov, V. P. Skulachev, and A. A. Starkov, *High Protonic Potential Actuates a Mechanism of Production of Reactive Oxygen Species in Mitochondria*, FEBS Lett **416**, 15 (1997).

[47] H. Sizek, A. Hamel, D. Deritei, S. Campbell, and E. Ravasz Regan, *Boolean Model of Growth Signaling, Cell Cycle and Apoptosis Predicts the Molecular Mechanism of Aberrant Cell Cycle Progression Driven by Hyperactive PI3K*, PLoS Comput. Biol. **15**, e1006402 (2019).

[48] I. Albert, J. Thakar, S. Li, R. Zhang, and R. Albert, *Boolean Network Simulations for Life Scientists*, Source Code Biol Med **3**, 16 (2008).

[49] yWorks GmbH, *yEd*, (2019).

[50] E. Sullivan, M. Harris, A. Bhatnagar, E. Guberman, I. Zonfa, and E. Ravasz Regan, *Boolean Modeling of Mechanosensitive Epithelial to Mesenchymal Transition and Its Reversal*, iScience **26**, 106321 (2023).

[51] E. Guberman, H. Sherief, and E. R. Regan, *Boolean Model of Anchorage Dependence and Contact Inhibition Points to Coordinated Inhibition but Semi-Independent Induction of Proliferation and Migration*, Comput Struct Biotechnol J **18**, 2145 (2020).

[52] M. Mann and K. Klemm, *Efficient Exploration of Discrete Energy Landscapes*, Physical Review E **83**, 011113 (2009).

[53] D. Deritei, W. C. Aird, M. Ercsey-Ravasz, and E. R. Regan, *Principles of Dynamical Modularity in Biological Regulatory Networks*, Sci Rep **6**, 21957 (2016).

[54] S. J. Yeung, J. Pan, and M.-H. Lee, *Roles of P53, MYC and HIF-1 in Regulating Glycolysis - the Seventh Hallmark of Cancer*, Cell Mol Life Sci **65**, 3981 (2008).

[55] T. Shi, D. M. K. van Soest, P. E. Polderman, B. M. T. Burgering, and T. B. Dansen, *DNA Damage and Oxidant Stress Activate P53 through Differential Upstream Signaling Pathways*, Free Radic Biol Med **172**, 298 (2021).

[56] U. S. Srinivas, B. W. Q. Tan, B. A. Vellayappan, and A. D. Jeyasekharan, *ROS and the DNA Damage Response in Cancer*, Redox Biol **25**, 101084 (2019).

[57] A. Tritarelli, E. Oricchio, M. Ciciarello, R. Mangiacasale, A. Palena, P. Lavia, S. Soddu, and E. Cundari, *P53 Localization at Centrosomes during Mitosis and Postmitotic Checkpoint Are ATM-Dependent and Require Serine 15 Phosphorylation*, Mol Biol Cell **15**, 3751 (2004).

[58] J. E. Toettcher, A. Loewer, G. J. Ostheimer, M. B. Yaffe, B. Tidor, and G. Lahav, *Distinct Mechanisms Act in Concert to Mediate Cell Cycle Arrest*, Proc. Natl. Acad. Sci. U.S.A. **106**, 785 (2009).

[59] R. Lipski, D. J. Lippincott, B. C. Durden, A. R. Kaplan, H. E. Keiser, J.-H. Park, and A. A. Levesque, *P53 Dimers Associate with a Head-to-Tail Response Element to Repress Cyclin B Transcription*, PLoS One **7**, e42615 (2012).

[60] K. H. Vousden and K. M. Ryan, *P53 and Metabolism*, Nat Rev Cancer **9**, 691 (2009).

[61] B. Alberts, A. Johnson, J. Lewis, D. Morgan, M. Raff, K. Roberts, and P. Walter, *Molecular Biology of the Cell*, 6th ed. (W.W. Norton & Company, 2017).

[62] H. Liang and W. F. Ward, *PGC-1alpha: A Key Regulator of Energy Metabolism*, Adv Physiol Educ **30**, 145 (2006).

[63] S. Wasiak, R. Zunino, and H. M. McBride, *Bax/Bak Promote Sumoylation of DRP1 and Its Stable Association with Mitochondria during Apoptotic Cell Death*, J Cell Biol **177**, 439 (2007).

[64] R.-S. Wang, A. Saadatpour, and R. Albert, *Boolean Modeling in Systems Biology: An Overview of Methodology and Applications.*, Physical Biology **9**, 055001 (2012).

[65] S. Kauffman, *Homeostasis and Differentiation in Random Genetic Control Networks*, Nature **224**, 177 (1969).

[66] Y. Suzuki-Karasaki, K. Fujiwara, K. Saito, M. Suzuki-Karasaki, T. Ochiai, and M. Soma, *Distinct Effects of TRAIL on the Mitochondrial Network in Human Cancer Cells and Normal Cells: Role of Plasma Membrane Depolarization*, Oncotarget **6**, 21572 (2015).

[67] T. L. Schmit, W. Zhong, V. Setaluri, V. S. Spiegelman, and N. Ahmad, *Targeted Depletion of Polo-like Kinase (Plk) 1 through Lentiviral shRNA or a Small-Molecule Inhibitor Causes Mitotic Catastrophe and Induction of Apoptosis in Human Melanoma Cells.*, The Journal of Investigative Dermatology **129**, 2843 (2009).

[68] Y. Ding, H. Gao, L. Zhao, X. Wang, and M. Zheng, *Mitofusin 2-Deficiency Suppresses Cell Proliferation through Disturbance of Autophagy*, PLoS One **10**, e0121328 (2015).

[69] W. Dai, G. Wang, J. Chwa, M. E. Oh, T. Abeywardana, Y. Yang, Q. A. Wang, and L. Jiang, *Mitochondrial Division Inhibitor (Mdivi-1) Decreases Oxidative Metabolism in Cancer*, Br J Cancer **122**, 1288 (2020).

[70] M. Shi, J. Hou, S. Shao, W. Liang, S. Wang, Y. Yang, Z. Guo, and F. Pan, *Short-Term Starvation Weakens the Efficacy of Cell Cycle Specific Chemotherapy Drugs through G1 Arrest*, Int J Mol Sci **24**, 2498 (2023).

[71] P. Mishra, V. Carelli, G. Manfredi, and D. C. Chan, *Proteolytic Cleavage of Opa1 Stimulates Mitochondrial Inner Membrane Fusion and Couples Fusion to Oxidative Phosphorylation*, Cell Metab **19**, 630 (2014).

[72] S. L. Spencer, S. D. Cappell, F.-C. Tsai, K. W. Overton, C. L. Wang, and T. Meyer, *The Proliferation-Quiescence Decision Is Controlled by a Bifurcation in CDK2 Activity at Mitotic Exit*, Cell **155**, 369 (2013).

[73] Y. Ren and H.-M. Shen, *Critical Role of AMPK in Redox Regulation under Glucose Starvation*, Redox Biol **25**, 101154 (2019).

[74] J. S. L. Ho, W. Ma, D. Y. L. Mao, and S. Benchimol, *P53-Dependent Transcriptional Repression of c-Myc Is Required for G1 Cell Cycle Arrest*, Mol Cell Biol **25**, 7423 (2005).

[75] H. Pan, Y. Zhu, W. Wei, S. Shao, and X. Rui, *Transcription Factor FoxM1 Is the Downstream Target of C-Myc and Contributes to the Development of Prostate Cancer*, World J Surg Oncol **16**, 59 (2018).

[76] K. W. Overton, S. L. Spencer, W. L. Noderer, T. Meyer, and C. L. Wang, *Basal P21 Controls Population Heterogeneity in Cycling and Quiescent Cell Cycle States*, Proc. Natl. Acad. Sci. U.S.A. **111**, E4386 (2014).

[77] G. Yao, T. J. Lee, S. Mori, J. R. Nevins, and L. You, *A Bistable Rb-E2F Switch Underlies the Restriction Point.*, Nat Cell Biol **10**, 476 (2008).

[78] S. M. Gross and P. Rotwein, *Unraveling Growth Factor Signaling and Cell Cycle Progression in Individual Fibroblasts.*, Journal of Biological Chemistry **291**, 14628 (2016).

[79] A. F. Serpico, F. Febbraro, C. Pisauro, and D. Grieco, *Compartmentalized Control of Cdk1 Drives Mitotic Spindle Assembly*, Cell Rep **38**, 110305 (2022).

[80] E. Ahn, P. Kumar, D. Mukha, A. Tzur, and T. Shlomi, *Temporal Fluxomics Reveals Oscillations in TCA Cycle Flux throughout the Mammalian Cell Cycle*, Molecular Systems Biology **13**, 953 (2017).

[81] L. Gheghiani, D. Loew, B. Lombard, J. Mansfeld, and O. Gavet, *PLK1 Activation in Late G2 Sets Up Commitment to Mitosis*, Cell Rep **19**, 2060 (2017).

[82] I. Sumara, J. F. Giménez-Abián, D. Gerlich, T. Hirota, C. Kraft, C. de la Torre, J. Ellenberg, and J.-M. Peters, *Roles of Polo-like Kinase 1 in the Assembly of Functional Mitotic Spindles.*, Current Biology : CB **14**, 1712 (2004).

[83] P. Lénárt, M. Petronczki, M. Steegmaier, B. Di Fiore, J. J. Lipp, M. Hoffmann, W. J. Rettig, N. Kraut, and J.-M. Peters, *The Small-Molecule Inhibitor BI 2536 Reveals Novel Insights into Mitotic Roles of Polo-like Kinase 1.*, Current Biology : CB **17**, 304 (2007).

[84] B. Lu, H. Mahmud, A. H. Maass, B. Yu, W. H. van Gilst, R. A. de Boer, and H. H. W. Silljé, *The Plk1 Inhibitor BI 2536 Temporarily Arrests Primary Cardiac Fibroblasts in Mitosis and Generates Aneuploidy in Vitro*, PLoS ONE **5**, e12963 (2010).

[85] M. E. Burkard, C. L. Randall, S. Larochelle, C. Zhang, K. M. Shokat, R. P. Fisher, and P. V. Jallepalli, *Chemical Genetics Reveals the Requirement for Polo-like Kinase 1 Activity in Positioning RhoA and Triggering Cytokinesis in Human Cells*, Proc. Natl. Acad. Sci. U.S.A. **104**, 4383 (2007).

[86] J. Rudner, V. Jendrossek, K. Lauber, P. T. Daniel, S. Wesselborg, and C. Belka, *Type I and Type II Reactions in TRAIL-Induced Apoptosis -- Results from Dose-Response Studies.*, Oncogene **24**, 130 (2005).

[87] D. A. Flusberg, J. Roux, S. L. Spencer, and P. K. Sorger, *Cells Surviving Fractional Killing by TRAIL Exhibit Transient but Sustainable Resistance and Inflammatory Phenotypes*, Mol. Biol. Cell **24**, 2186 (2013).

[88] H. Matsuzaki, B. M. Schmied, A. Ulrich, J. Standop, M. B. Schneider, S. K. Batra, K. S. Picha, and P. M. Pour, *Combination of Tumor Necrosis Factor-Related Apoptosis-Inducing Ligand (TRAIL) and Actinomycin D Induces Apoptosis Even in TRAIL-Resistant Human Pancreatic Cancer Cells.*, Clinical Cancer Research : An Official Journal of the American Association for Cancer Research **7**, 407 (2001).

[89] M. Kim, J. Liao, M. L. Dowling, K. R. Voong, S. E. Parker, S. Wang, W. S. El-Deiry, and G. D. Kao, *TRAIL Inactivates the Mitotic Checkpoint and Potentiates Death Induced by Microtubule-Targeting Agents in Human Cancer Cells*, Cancer Res. **68**, 3440 (2008).

[90] S. Victorelli et al., *Apoptotic Stress Causes mtDNA Release during Senescence and Drives the SASP*, Nature **622**, 627 (2023).

[91] T. Yamamori, S. Ike, T. Bo, T. Sasagawa, Y. Sakai, M. Suzuki, K. Yamamoto, M. Nagane, H. Yasui, and O. Inanami, *Inhibition of the Mitochondrial Fission Protein Dynamin-Related Protein 1 (Drp1) Impairs Mitochondrial Fission and Mitotic Catastrophe after x-Irradiation*, Mol Biol Cell **26**, 4607 (2015).

[92] C. Dai, F. Sun, C. Zhu, and X. Hu, *Tumor Environmental Factors Glucose Deprivation and Lactic Acidosis Induce Mitotic Chromosomal Instability--an Implication in Aneuploid Human Tumors*, PLoS One **8**, e63054 (2013).

[93] J. Du, H. Li, J. Song, T. Wang, Y. Dong, A. Zhan, Y. Li, and G. Liang, *AMPK Activation Alleviates Myocardial Ischemia-Reperfusion Injury by Regulating Drp1-Mediated Mitochondrial Dynamics*, Front Pharmacol **13**, 862204 (2022).

[94] M. Liesa, B. Borda-d'Agua, G. Medina-Gómez, C. J. Lelliott, J. C. Paz, M. Rojo, M. Palacín, A. Vidal-Puig, and A. Zorzano, *Mitochondrial Fusion Is Increased by the Nuclear Coactivator PGC-1beta*, PLoS One **3**, e3613 (2008).

[95] S. M. Jin and R. J. Youle, *PINK1- and Parkin-Mediated Mitophagy at a Glance*, J Cell Sci **125**, 795 (2012).

[96] I. Martínez-Reyes and N. S. Chandel, *Mitochondrial TCA Cycle Metabolites Control Physiology and Disease*, Nat Commun **11**, 102 (2020).

[97] J. Bastin, M. Sroussi, I. Nemazanyy, P. Laurent-Puig, S. Mouillet-Richard, and F. Djouadi, *Downregulation of Mitochondrial Complex I Induces ROS Production in Colorectal Cancer Subtypes That Differently Controls Migration*, J Transl Med **21**, 522 (2023).

[98] M. Sinkala, *Mutational Landscape of Cancer-Driver Genes across Human Cancers*, Sci Rep **13**, 12742 (2023).

[99] R. Summer, H. Shaghaghi, D. Schriner, W. Roque, D. Sales, K. Cuevas-Mora, V. Desai, A. Bhushan, M. I. Ramirez, and F. Romero, *Activation of the mTORC1/PGC-1 Axis Promotes Mitochondrial Biogenesis and Induces Cellular Senescence in the Lung Epithelium*, Am J Physiol Lung Cell Mol Physiol **316**, L1049 (2019).

[100] M. Morita et al., *mTOR Controls Mitochondrial Dynamics and Cell Survival via MTFP1*, Mol Cell **67**, 922 (2017).

[101] C. M. Beausejour, *Reversal of Human Cellular Senescence: Roles of the P53 and P16 Pathways*, The EMBO Journal **22**, 4212 (2003).

[102] Q. Li, Y. Zhang, J. Fu, L. Han, L. Xue, C. Lv, P. Wang, G. Li, and T. Tong, *FOXA1 Mediates P16(INK4a) Activation during Cellular Senescence*, EMBO J **32**, 858 (2013).

[103] H. Li, W. Wang, X. Liu, K. E. Paulson, A. S. Yee, and X. Zhang, *Transcriptional Factor HBP1 Targets P16INK4A, Upregulating Its Expression and Consequently Is Involved in Ras-Induced Premature Senescence*, Oncogene **29**, 5083 (2010).

[104] Y. Ito, M. Hoare, and M. Narita, *Spatial and Temporal Control of Senescence*, Trends Cell Biol **27**, 820 (2017).

[105] J. Stewart-Ornstein et al., *P53 Dynamics Vary between Tissues and Are Linked with Radiation Sensitivity*, Nat Commun **12**, 898 (2021).

[106] R. Rossignol, B. Faustin, C. Rocher, M. Malgat, J.-P. Mazat, and T. Letellier, *Mitochondrial Threshold Effects*, Biochem J **370**, 751 (2003).

[107] D. Aw, A. B. Silva, and D. B. Palmer, *Immunosenescence: Emerging Challenges for an Ageing Population*, Immunology **120**, 435 (2007).

[108] J. C. Acosta et al., *A Complex Secretory Program Orchestrated by the Inflammasome Controls Paracrine Senescence*, Nat Cell Biol **15**, 978 (2013).

[109] O. Karin, A. Agrawal, Z. Porat, V. Krizhanovsky, and U. Alon, *Senescent Cell Turnover Slows with Age Providing an Explanation for the Gompertz Law*, Nat Commun **10**, 5495 (2019).

[110] C. Lawless, D. Jurk, C. S. Gillespie, D. Shanley, G. Saretzki, T. von Zglinicki, and J. F. Passos, *A Stochastic Step Model of Replicative Senescence Explains ROS Production Rate in Ageing Cell Populations*, PLoS One **7**, e32117 (2012).

[111] S. Go, T. T. Kramer, A. J. Verhoeven, R. P. J. Oude Elferink, and J.-C. Chang, *The Extracellular Lactate-to-Pyruvate Ratio Modulates the Sensitivity to Oxidative Stress-Induced Apoptosis via the Cytosolic NADH/NAD+ Redox State*, Apoptosis **26**, 38 (2021).

Supplementary Materials

Supplementary Table 1 -- Large (107-page), formatted and referenced table describing the biological evidence behind each node, link, and logic gate of our model, organized by regulatory module.

Supplementary Figures and File list – *MiDAS__Supp_Figures_And_Files_list.pdf* file containing 16 supplementary figures with captions, followed by a list of supplementary files with brief descriptions (16 files).

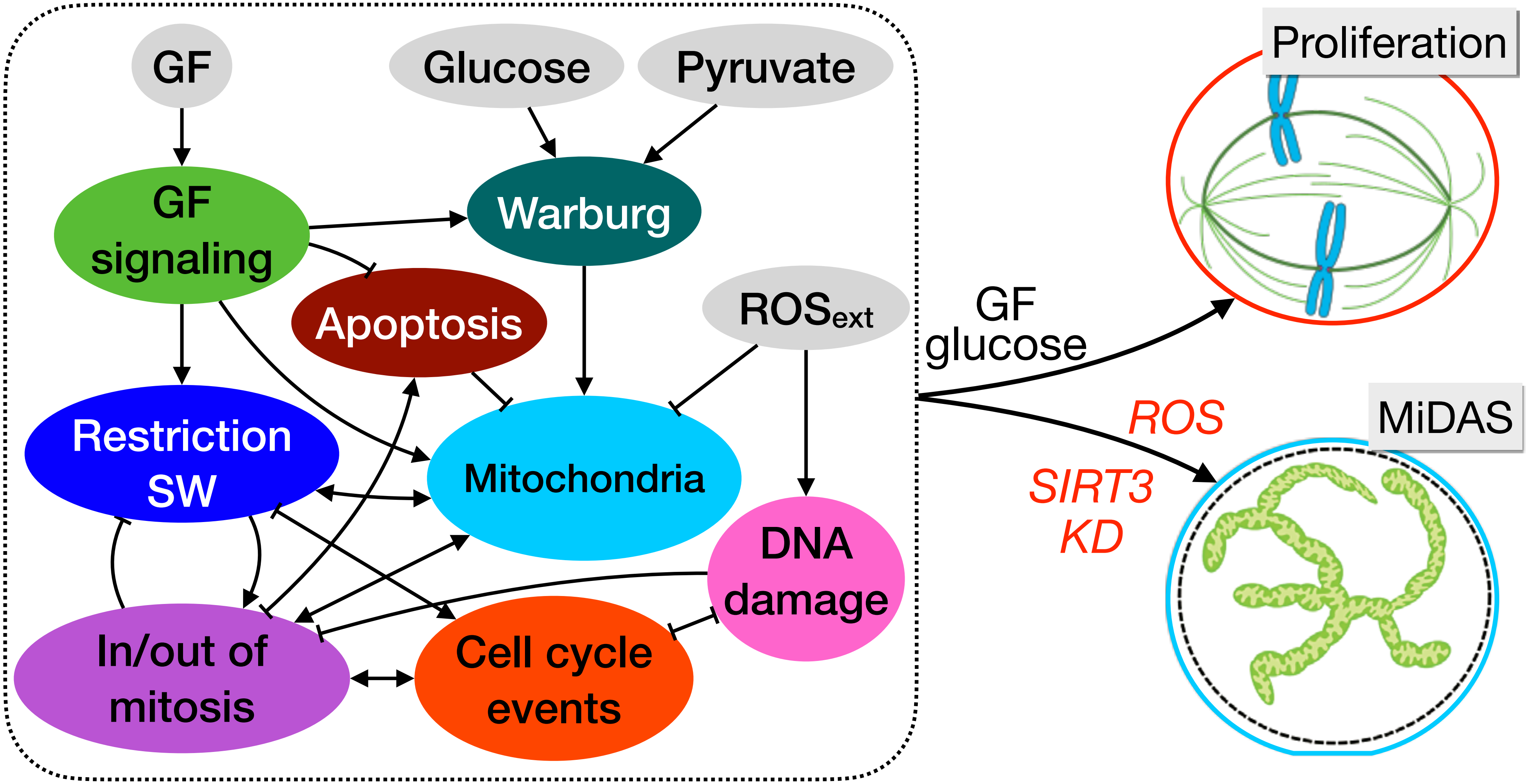
GF
Glucose
Pyruvate
GF signaling
Warburg
Apoptosis
ROSext
Restriction SW
Mitochondria
DNA damage
In/out of mitosis
Cell cycle events
GF glucose
ROS
SIRT3 KD
Proliferation
MiDAS

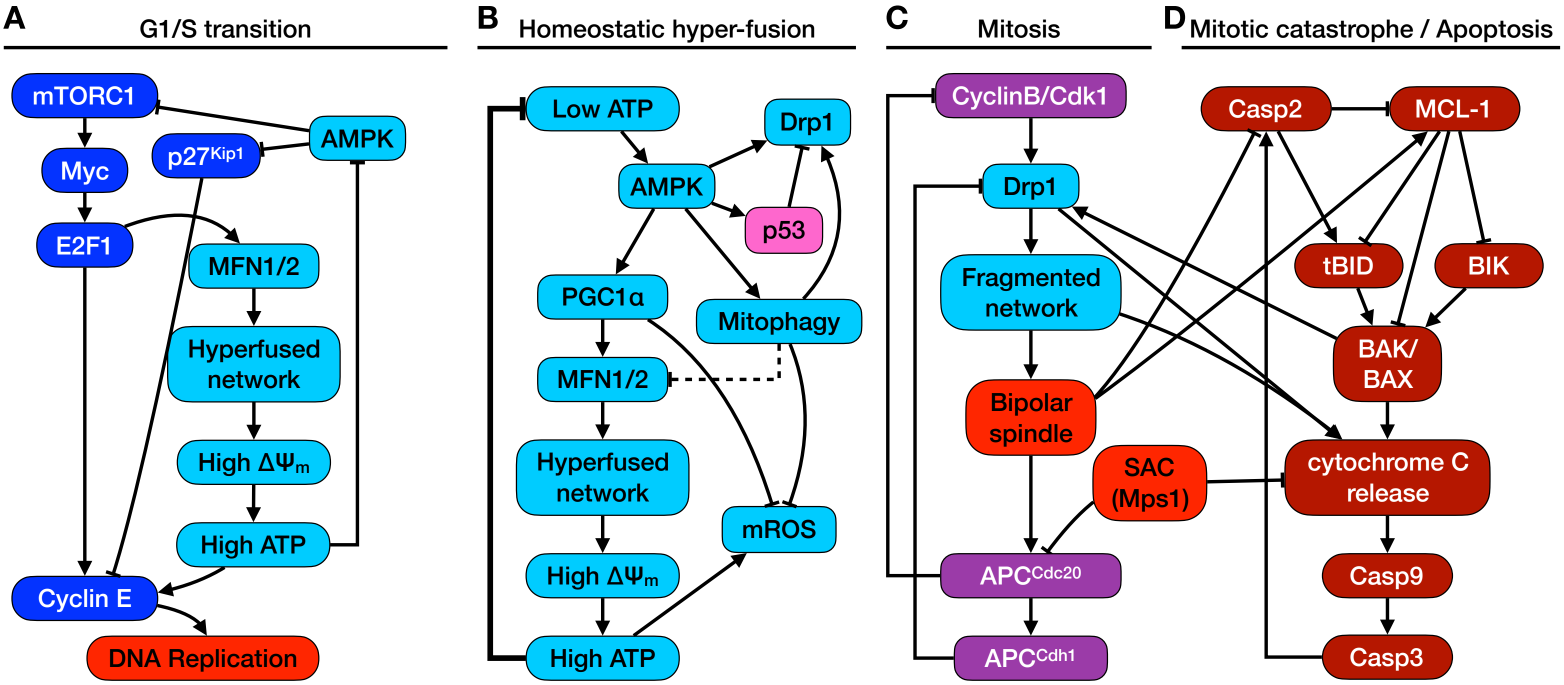
A
G1/S transition
mTORC1
AMPK
Myc
$p27^{Kip1}$
E2F1
MFN1/2
Hyperfused network
High $\Delta\Psi_m$
High ATP
Cyclin E
DNA Replication
B
Homeostatic hyper-fusion
Low ATP
Drp1
AMPK
p53
PGC1α
Mitophagy
MFN1/2
Hyperfused network
mROS
High $\Delta\Psi_m$
High ATP
C
Mitosis
CyclinB/Cdk1
Drp1
Fragmented network
Bipolar spindle
SAC (Mps1)
APC^{Cdc20}
APC^{Cdh1}
D
Mitotic catastrophe / Apoptosis
Casp2
MCL-1
tBID
BIK
BAK/ BAX
cytochrome C release
Casp9
Casp3

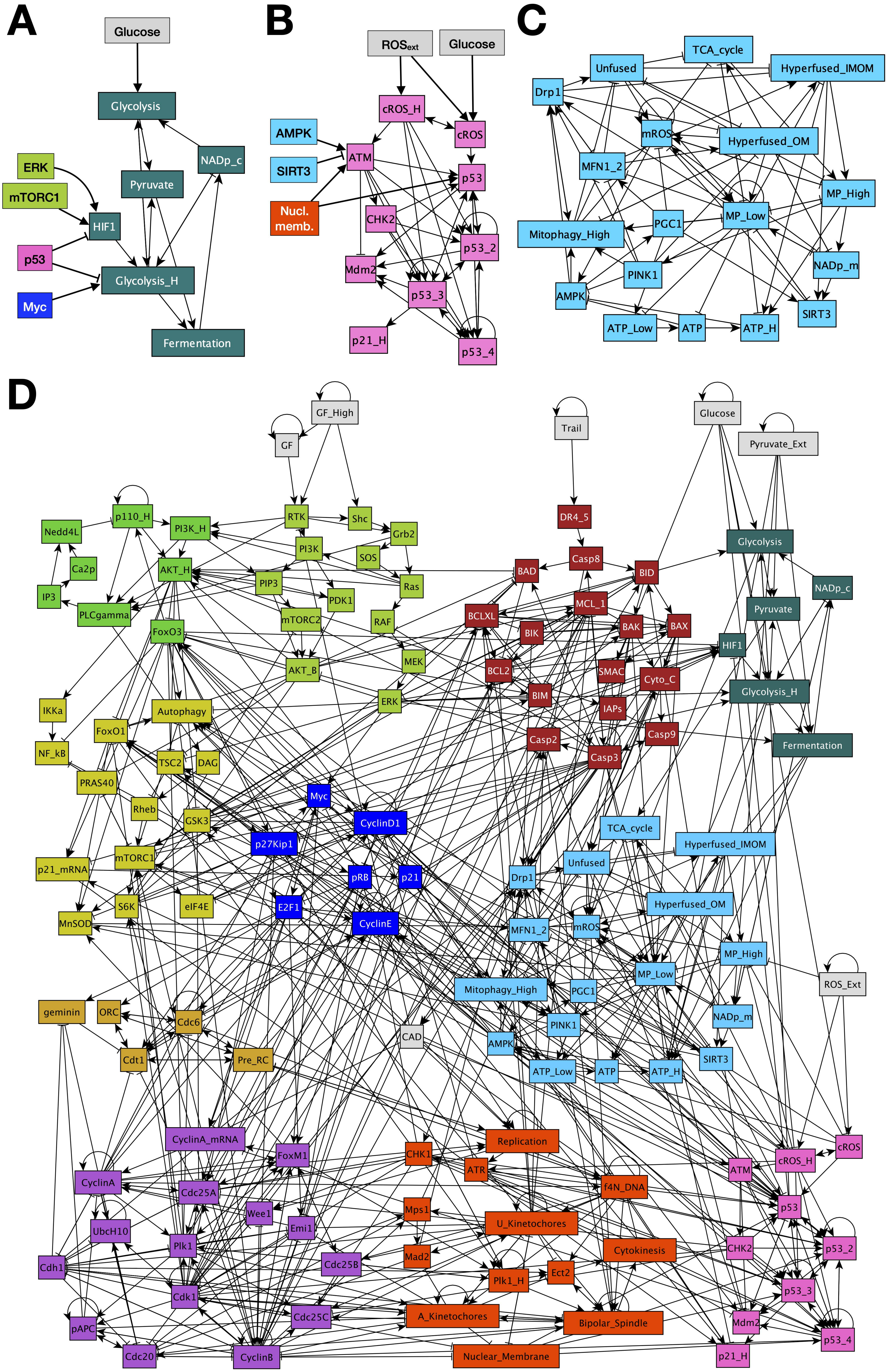
A
Glucose
Glycolysis
NADp_c
Pyruvate
ERK
mTORC1
HIF1
p53
Glycolysis_H
Myc
Fermentation
B
ROSext
Glucose
cROS_H
cROS
AMPK
SIRT3
ATM
p53
Nucl. memb.
CHK2
p53_2
Mdm2
p53_3
p21_H
p53_4
C
TCA_cycle
Unfused
Hyperfused_IMOM
Drp1
mROS
Hyperfused_OM
MFN1_2
MP_High
PGC1
MP_Low
Mitophagy_High
PINK1
NADp_m
AMPK
SIRT3
ATP_Low
ATP
ATP_H
D
GF_High
GF
Trail
Glucose
Pyruvate_Ext
p110_H
Nedd4L
PI3K_H
RTK
Shc
Grb2
PI3K
SOS
Ca2p
AKT_H
PIP3
Ras
IP3
PDK1
PLCgamma
mTORC2
RAF
FoxO3
AKT_B
MEK
ERK
IKKa
Autophagy
NF_kB
FoxO1
TSC2
DAG
PRAS40
Rheb
GSK3
Myc
CyclinD1
p27Kip1
mTORC1
p21_mRNA
pRB
p21
S6K
eIF4E
E2F1
CyclinE
MnSOD
DR4_5
Casp8
BAD
BID
Glycolysis
NADp_c
BCLXL
MCL_1
BIK
BAK
BAX
Pyruvate
HIF1
BCL2
SMAC
Cyto_C
Glycolysis_H
BIM
IAPs
Casp2
Casp9
Casp3
Fermentation
TCA_cycle
Hyperfused_IMOM
Unfused
Drp1
Hyperfused_OM
MFN1_2
mROS
MP_High
MP_Low
Mitophagy_High
PGC1
ROS_Ext
NADp_m
PINK1
AMPK
CAD
ATP_Low
ATP
ATP_H
SIRT3
geminin
ORC
Cdc6
Cdt1
Pre_RC
CyclinA_mRNA
FoxM1
CHK1
Replication
ATR
f4N_DNA
ATM
cROS_H
cROS
CyclinA
Cdc25A
Wee1
Emi1
Mps1
U_Kinetochores
p53
UbcH10
Plk1
Cdc25B
Mad2
Cytokinesis
CHK2
p53_2
Cdh1
Plk1_H
Ect2
p53_3
Cdk1
Cdc25C
A_Kinetochores
Bipolar_Spindle
Mdm2
pAPC
p53_4
Cdc20
CyclinB
Nuclear_Membrane
p21_H

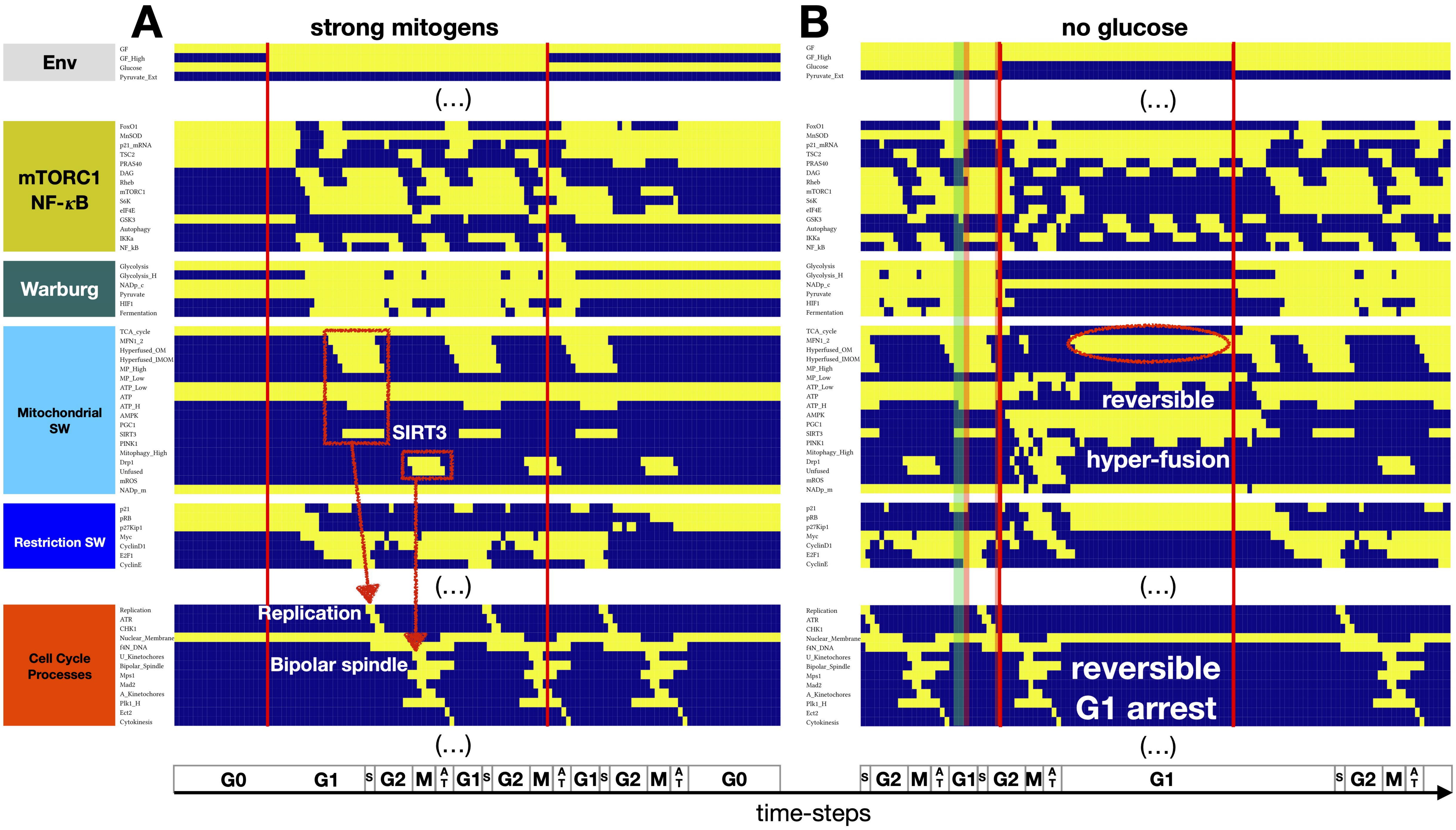
A
strong mitogens
B
no glucose
Env
GF
GF_High
Glucose
Pyruvate_Ext
(…)
mTORC1
NF-κB
FoxO1
MnSOD
p21_mRNA
TSC2
PRAS40
DAG
Rheb
mTORC1
S6K
eIF4E
GSK3
Autophagy
IKKa
NF_kB
Warburg
Glycolysis
Glycolysis_H
NADp_c
Pyruvate
HIF1
Fermentation
Mitochondrial SW
TCA_cycle
MFN1_2
Hyperfused_OM
Hyperfused_IMOM
MP_High
MP_Low
ATP_Low
ATP
ATP_H
AMPK
PGC1
SIRT3
PINK1
Mitophagy_High
Drp1
Unfused
mROS
NADp_m
SIRT3
Restriction SW
p21
pRB
p27Kip1
Myc
CyclinD1
E2F1
CyclinE
(…)
Cell Cycle Processes
Replication
ATR
CHK1
Nuclear_Membrane
f4N_DNA
U_Kinetochores
Bipolar_Spindle
Mps1
Mad2
A_Kinetochores
Plk1_H
Ect2
Cytokinesis
Replication
Bipolar spindle
(…)
G0
G1
S
G2
M
A T
G1
S
G2
M
A T
G1
S
G2
M
A T
G0
reversible
hyper-fusion
reversible
G1 arrest
S
G2
M
A T
G1
S
G2
M
A T
G1
S
G2
M
A T
time-steps

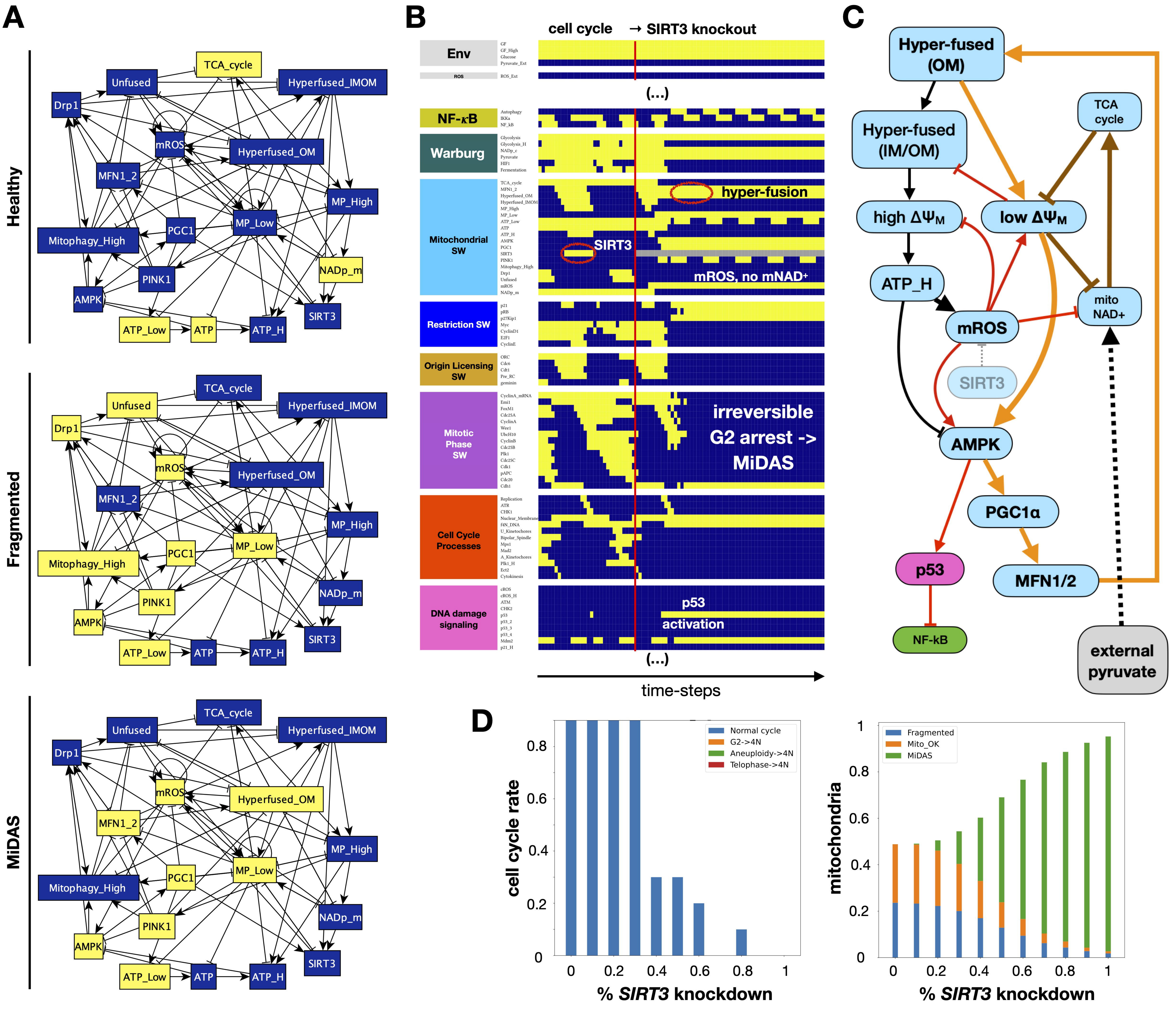
A
Healthy
Fragmented
MiDAS
TCA_cycle
Unfused
Hyperfused_IMOM
Drp1
mROS
Hyperfused_OM
MFN1_2
MP_High
MP_Low
PGC1
Mitophagy_High
NADp_m
PINK1
AMPK
SIRT3
ATP_Low
ATP
ATP_H
B
cell cycle
→ SIRT3 knockout
Env
GF
GF_High
Glucose
Pyruvate_Ext
ROS
ROS_Ext
(...)
NF-κB
Autophagy
IKKa
NF_kB
Warburg
Glycolysis
Glycolysis_H
NADp_c
Pyruvate
HIF1
Fermentation
Mitochondrial SW
TCA_cycle
MFN1_2
Hyperfused_OM
Hyperfused_IMOM
MP_High
MP_Low
ATP_Low
ATP
ATP_H
AMPK
PGC1
SIRT3
PINK1
Mitophagy_High
Drp1
Unfused
mROS
NADp_m
hyper-fusion
SIRT3
mROS, no mNAD+
Restriction SW
p21
pRB
p27Kip1
Myc
CyclinD1
E2F1
CyclinE
Origin Licensing SW
ORC
Cdc6
Cdt1
Pre_RC
geminin
Mitotic Phase SW
CyclinA_mRNA
Emi1
FoxM1
Cdc25A
CyclinA
Wee1
UbcH10
CyclinB
Cdc25B
Plk1
Cdc25C
Cdk1
pAPC
Cdc20
Cdh1
irreversible G2 arrest -> MiDAS
Cell Cycle Processes
Replication
ATR
CHK1
Nuclear_Membrane
f4N_DNA
U_Kinetochores
Bipolar_Spindle
Mps1
Mad2
A_Kinetochores
Plk1_H
Ect2
Cytokinesis
DNA damage signaling
cROS
cROS_H
ATM
CHK2
p53
p53_2
p53_3
p53_4
Mdm2
p21_H
p53 activation
(...)
time-steps
C
Hyper-fused (OM)
Hyper-fused (IM/OM)
TCA cycle
high $\Delta\Psi_M$
low $\Delta\Psi_M$
ATP_H
mROS
mito NAD+
SIRT3
AMPK
PGC1α
p53
MFN1/2
NF-kB
external pyruvate
D
cell cycle rate
0
0.2
0.4
0.6
0.8
% SIRT3 knockdown
0
0.2
0.4
0.6
0.8
1
Normal cycle
G2->4N
Aneuploidy->4N
Telophase->4N
mitochondria
0
0.2
0.4
0.6
0.8
1
% SIRT3 knockdown
0
0.2
0.4
0.6
0.8
1
Fragmented
Mito_OK
MiDAS

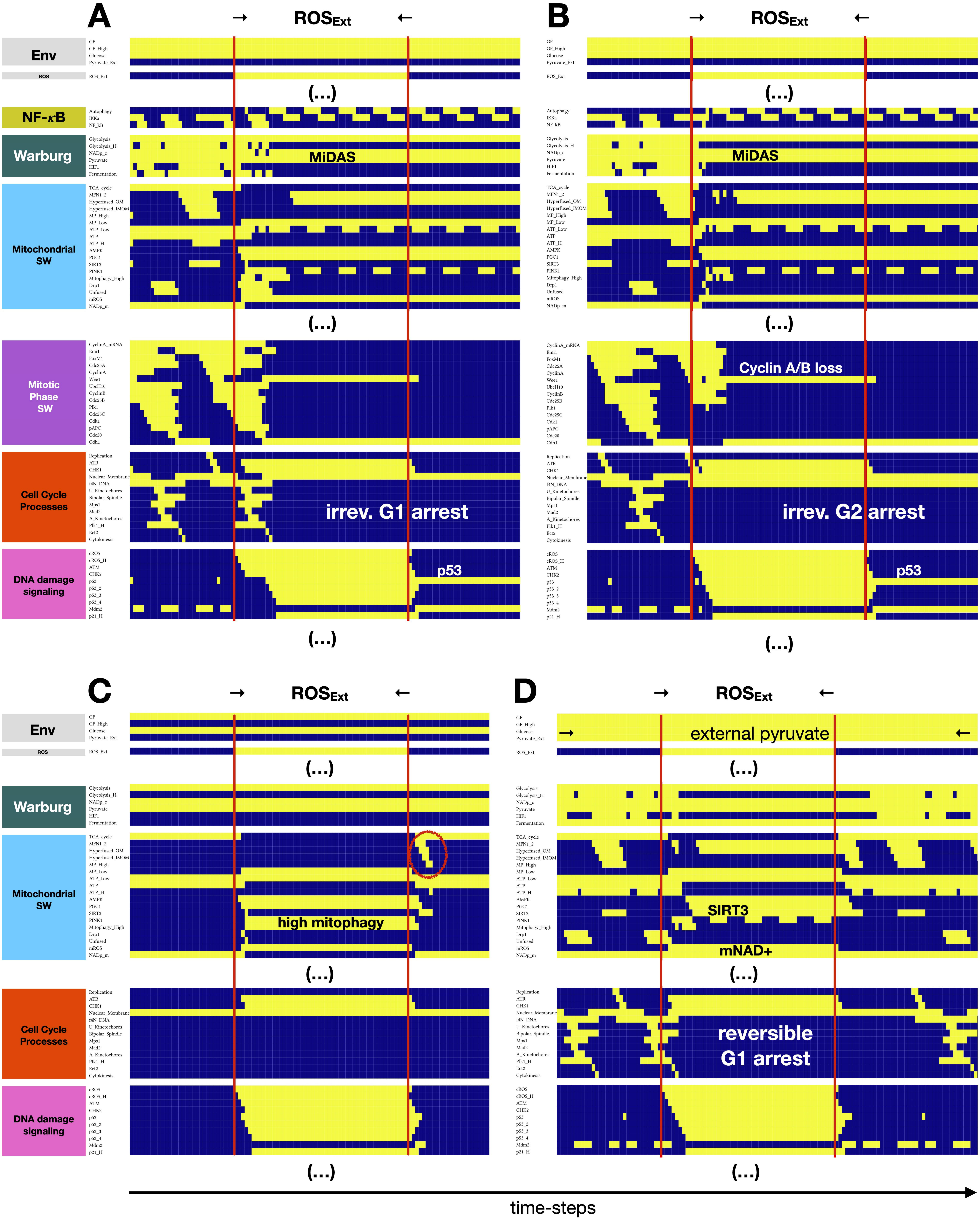A
→ ROSExt ←
Env
GF
GF_High
Glucose
Pyruvate_Ext
ROS
ROS_Ext
(...)
NF-κB
Autophagy
IKKa
NF_kB
Warburg
Glycolysis
Glycolysis_H
NADp_c
Pyruvate
HIF1
Fermentation
MiDAS
Mitochondrial SW
TCA_cycle
MFN1_2
Hyperfused_OM
Hyperfused_IMOM
MP_High
MP_Low
ATP_Low
ATP
ATP_H
AMPK
PGC1
SIRT3
PINK1
Mitophagy_High
Drp1
Unfused
mROS
NADp_m
(...)
Mitotic Phase SW
CyclinA_mRNA
Emi1
FoxM1
Cdc25A
CyclinA
Wee1
UbcH10
CyclinB
Cdc25B
Plk1
Cdc25C
Cdk1
pAPC
Cdc20
Cdh1
Cell Cycle Processes
Replication
ATR
CHK1
Nuclear_Membrane
f4N_DNA
U_Kinetochores
Bipolar_Spindle
Mps1
Mad2
A_Kinetochores
Plk1_H
Ect2
Cytokinesis
irrev. G1 arrest
DNA damage signaling
cROS
cROS_H
ATM
CHK2
p53
p53_2
p53_3
p53_4
Mdm2
p21_H
p53
(...)
B
→ ROSExt ←
(...)
MiDAS
(...)
Cyclin A/B loss
irrev. G2 arrest
p53
(...)
C
→ ROSExt ←
Env
ROS
(...)
Warburg
Mitochondrial SW
high mitophagy
(...)
Cell Cycle Processes
DNA damage signaling
(...)
D
→ ROSExt ←
→ external pyruvate ←
(...)
SIRT3
mNAD+
(...)
reversible G1 arrest
(...)
time-steps

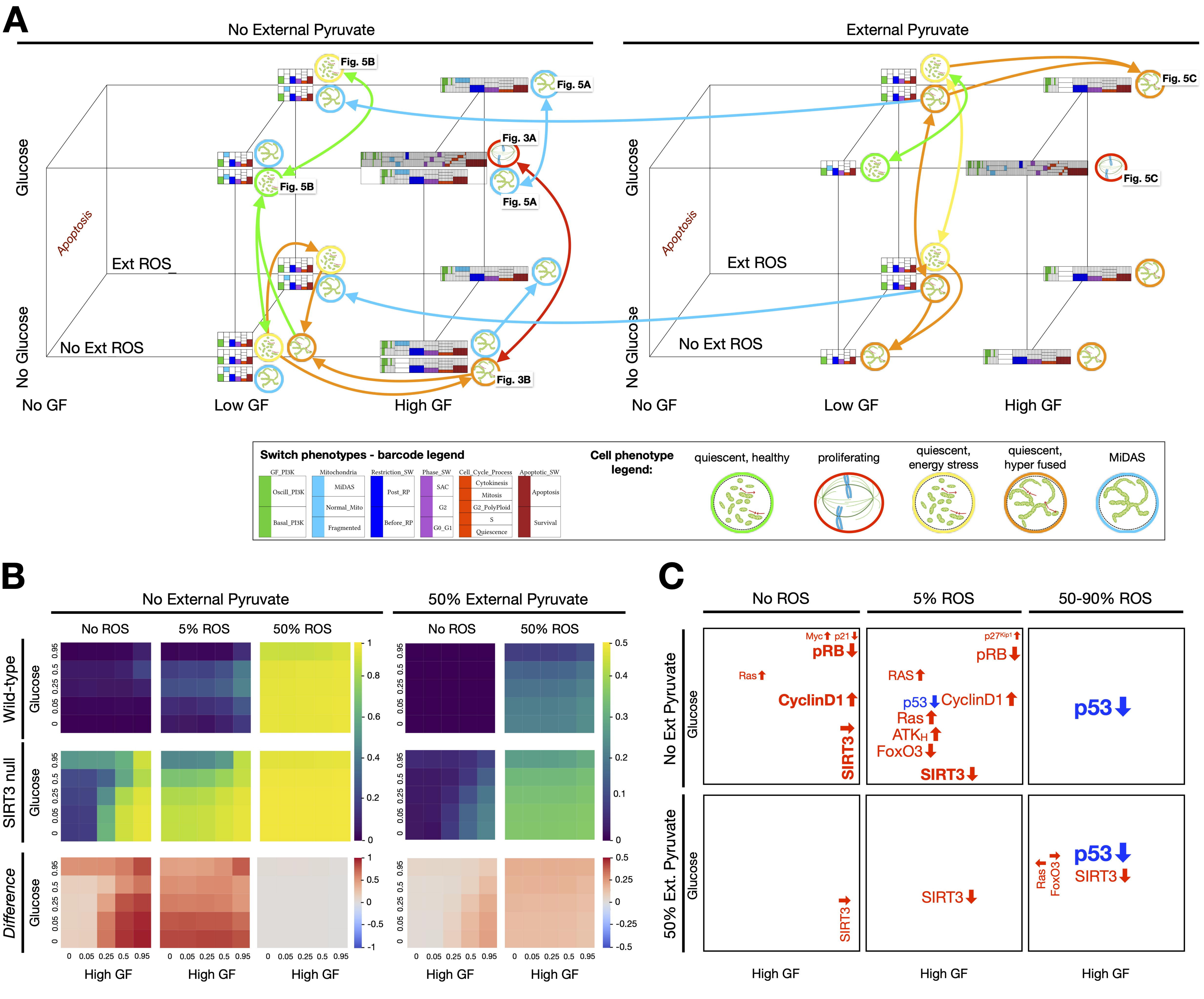
A
No External Pyruvate
External Pyruvate
Fig. 5B
Fig. 5A
Fig. 3A
Fig. 5B
Fig. 5A
Fig. 3B
Fig. 5C
Fig. 5C
Glucose
No Glucose
Apoptosis
Ext ROS
No Ext ROS
No GF
Low GF
High GF
Switch phenotypes - barcode legend
GF_PI3K
Oscill_PI3K
Basal_PI3K
Mitochondria
MiDAS
Normal_Mito
Fragmented
Restriction_SW
Post_RP
Before_RP
Phase_SW
SAC
G2
G0_G1
Cell_Cycle_Process
Cytokinesis
Mitosis
G2_PolyPloid
S
Quiescence
Apoptotic_SW
Apoptosis
Survival
Cell phenotype legend:
quiescent, healthy
proliferating
quiescent, energy stress
quiescent, hyper fused
MiDAS
B
No External Pyruvate
50% External Pyruvate
No ROS
5% ROS
50% ROS
No ROS
50% ROS
Wild-type
SIRT3 null
Difference
Glucose
0 0.05 0.25 0.5 0.95
High GF
1 0.8 0.6 0.4 0.2 0
0.5 0.4 0.3 0.2 0.1 0
1 0.5 0 -0.5 -1
0.5 0.25 0 -0.25 -0.5
C
No ROS
5% ROS
50-90% ROS
No Ext Pyruvate
50% Ext. Pyruvate
Glucose
Myc↑ p21↓
pRB↓
Ras↑
CyclinD1↑
SIRT3→
p27Kip1↑
pRB↓
RAS↑
p53↓ CyclinD1↑
Ras↑
ATKH↑
FoxO3↓
SIRT3↓
p53↓
SIRT3→
SIRT3↓
Ras↑
FoxO3→
p53↓
SIRT3↓
High GF